THE JOURNAL OF PHYSICAL CHEMISTRY C
A JOURNAL OF THE AMERICAN CHEMICAL SOCIETY

pubs.acs.org/JPCC

Article

Theoretical and Experimental Characterization of Adsorbed CO and NO on γ-Al_2O_3-Supported Rh Nanoparticles

Alexander J. Hoffman, Chithra Asokan, Nicholas Gadinas, Pavlo Kravchenko, Andrew "Bean" Getsoian, Phillip Christopher,* and David Hibbitts*

Cite This: https://doi.org/10.1021/acs.jpcc.1c05160

Read Online

ACCESS | Metrics & More | Article Recommendations | Supporting Information

ABSTRACT: Rh active sites are critical for NO_x reduction in automotive three-way catalysts. Low Rh loadings used in industrial catalysts lead to a mixture of small nanoparticles and single-atom Rh species. This active-site heterogeneity complicates the interpretation of characterization and reactivity, making the development of structure–function relationships challenging. Density functional theory (DFT) investigations of Rh catalysts often employ flat, periodic surfaces, which lack the curvature of oxide-supported Rh nanoparticle surfaces, raising questions about the validity of periodic surface model systems. Here, we combine DFT with probe molecule Fourier transform infrared (FTIR) spectroscopy and high-resolution scanning transmission electron microscopy of supported Rh catalysts synthesized to insure against the *in situ* formation of single-atom Rh species to compare periodic and nanoparticle DFT models for describing the interaction of CO and NO with supported Rh nanoparticles. We focus on comparing the behavior of model systems—Rh(111) and a 201-atom cubo-octahedral Rh nanoparticle (Rh_{201}; ~1.7 nm diameter)—to explain the behavior of CO and NO bound to Rh nanoparticles with an average particle diameter of ~2.6 nm. Our DFT calculations indicate that CO* occupies a mixture of threefold and atop modes on Rh(111), saturating at 0.56 ML CO* (473 K, 1 bar), while CO* saturates Rh_{201} near 1 ML. Similarly, NO* binds to threefold sites and saturates the Rh(111) surface at 0.67 ML but saturates the Rh_{201} particle surface at 1.38 ML, indicating that more NO* binds than there are Rh_{surf} atoms. Moreover, the adlayers on the Rh_{201} particle contain predominantly atop-bound CO*, with bridge CO* possible on particle edges and predominantly threefold NO* with bridge- and atop-bound NO* bound to edges and corners. These binding modes and higher coverages are made possible by the curvature of these nanoparticles and by the expansion of surface metal–metal bonds—neither of which can occur on Rh(111)—which together permit the adlayer to laterally relax, reducing internal strain. FTIR data for CO* on 10 wt % Rh/γ-Al_2O_3 show predominantly atop binding modes (2067 cm^{-1}) with small broad peaks near bridge (1955 cm^{-1}) and threefold (1865 cm^{-1}) regions. Meanwhile, NO* FTIR spectroscopy also shows a mixture of atop (1820 cm^{-1}) and threefold (1685 cm^{-1}) NO* features, with similar features observed at reaction conditions (5 mbar NO, 1 mbar CO, 478 K), indicating that NO* dominates Rh surfaces during catalysis. Frequency calculations on these adlayers of Rh_{201} particles yield dominant frequencies that more closely resemble those observed in FTIR spectra and demonstrate how coverage and dipole–dipole coupling affect vibrational frequencies with surface curvature. Taken together, these results indicate that the Rh surface curvature alters the structure and spectral characteristics of NO* and CO* for Rh nanoparticles of ~2.6 nm diameter, which must be accurately reflected in DFT models.

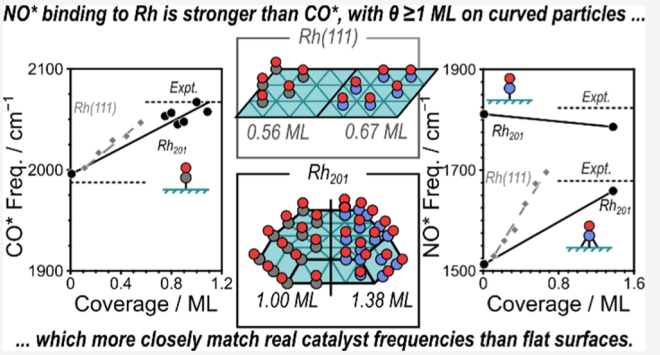

1. INTRODUCTION

NO_x species (x = 1, 2) are pollutants present in the exhaust streams of combustion engines in automobiles.[1] Three-way catalysts (TWCs) comprising Pd, Pt, and Rh reduce NO_x to N_2, as well as undesired N_2O and NH_3,[2−5] by reacting with reductants in the exhaust stream—primarily CO but also H_2, NH_3, and uncombusted hydrocarbons.[1,6−9] TWCs have significantly reduced pollution since their introduction in 1975, with total atmospheric pollution in the United States decreasing by 68% since 1980.[10] As targets for pollution reduction grow more aggressive, TWCs continue to attract significant attention.[2,4,5] Unresolved challenges include poor activity and selectivity to N_2 at low temperatures (<600 K) during engine startup and the high costs of the required precious metals.[11]

Received: June 11, 2021
Revised: August 11, 2021

Rh is more active during NO_x reduction by CO than other Pt-group metals in TWCs, leading to its ubiquitous use in TWC formulations.[12,13] Despite extensive investigation, Rh-catalyzed NO_x reduction mechanisms remain incompletely understood. Many reactions are plausible, with relative rates determined by the coverages of chemisorbed NO*, CO*, vacant sites (*), and other coreactants or intermediates. For example, during NO reduction by CO, the direct activation of adsorbed NO (NO*) on a surface

$$NO^* + * \rightarrow N^* + O^* \quad (1)$$

requires the presence of both NO* on the surface and a nearby vacancy that can accommodate O* upon dissociation. Alternatively, NO* activation can be assisted by CO* to form CO_2

$$NO^* + CO^* \rightarrow N^* + * + CO_2(g) \quad (2)$$

or to form an isocyanate

$$NO^* + CO^* \rightarrow O^* + NCO^* \quad (3)$$

among other possibilities. Each of these reactions depends on the relative concentrations of vacancies (*), NO*, CO*, and other intermediates. These effects of coverage are ubiquitous in heterogeneous catalysis but remain poorly understood for this chemistry, in which two strongly bound reactants (NO* and CO*) compete for sites. Therefore, a clear understanding of the coverages of the most abundant surface intermediates (MASI) and the saturation coverages of these catalysts (θ_{sat}) is key to understanding catalytic behavior of Rh during NO_x reduction.

Insights into differences in intermolecular interactions occurring in adlayers on Rh single crystals and particles can be informed by vibrational spectroscopy. Fourier-transform infrared (FTIR) spectroscopy can be used to infer CO* binding geometries and relative coverages on Rh and other metal surfaces.[14] Well-defined single-crystal surfaces under highly controlled ultrahigh vacuum conditions serve as a benchmark for CO* stretch frequencies. On Rh(111), CO* vibrational modes at ~2040−2070 cm^{-1} corresponding to linear atop CO* appear below 0.4 ML and modes at 1820−1860 cm^{-1}, indicating threefold-bound CO*, appear above 0.5 ML and up to the θ_{sat} of ~0.7 ML (95−150 K, 10^{-9} to 10^{-5} Torr CO).[15−20] The frequency of these bands increases with increasing coverage because of a combination of electrostatic repulsion and dipole−dipole coupling between neighboring CO*.[15,16,19,21,22] Furthermore, the areas of these bands increase nonlinearly with coverage because of energy transfer occurring to higher energy normal modes that dominate surfaces at high CO* coverage and which often have lower extinction coefficients.[23,24]

Similarly, NO probe-molecule vibrational spectroscopy can be used to characterize surfaces by itself or in combination with CO to assess these surfaces in environments more like those relevant to automotive catalysis. Infrared (IR) spectra of NO* on Rh(111) reveal stretching frequencies at 1479−1650 and 1816−1867 cm^{-1} corresponding to threefold and atop binding geometries, with frequencies generally increasing with coverage.[25−27] Similar electron energy loss spectroscopy (EELS) data—which can also identify characteristic N−O stretching frequencies for NO* and, thus, binding modes—indicate similar frequencies for threefold (1480−1630 cm^{-1}) and atop (1840 cm^{-1}) NO*.[28] Unlike CO*, NO* can be activated on Rh surfaces to form N_2 or N_2O at low coverages, rather than simply desorb.[28−30] As such, temperature-programmed desorption (TPD) results show NO desorbs from NO* saturated Rh(111) near 400 K, followed by N_2 desorption near 600 K and O_2 desorption above 1000 K.[20,28] The formation of N_2 and O_2 during these TPD studies indicates that some of the NO* initially bound to the surface reacts prior to desorption at 400 K. When exposed to equal mixtures of CO and NO, NO* dominates the surface of Rh(111) (1.1 kPa CO and NO, 523−673 K), but CO* can begin to occupy more of the surface above 623 K at higher CO/NO ratios, representative of those during automotive catalysis (0.6 kPa CO, 0.1 kPa NO, 523−673 K).[31] These surface science studies indicate that Rh surfaces are more selective to N_2O when reacting with CO at low temperature (<635 K);[31−33] however, Rh is highly selective to the preferred N_2 product at high-temperature operating conditions in automotive exhaust streams.[12] Notably, Rh catalysts are typically prepared in low loadings on oxide supports in automobile industrial catalysts, and therefore, realistic Rh active sites are on the surface of small supported nanoparticles, or even atomically dispersed species, rather than extended single-crystal surfaces.[11,34] The influence of the Rh structure (single crystals or small nanoparticles) on reactivity is highlighted by the substantially different behavior of single-crystal Rh(111) surfaces from supported Rh/Al_2O_3 catalysts during NO−CO reactions, with Rh(111) forming CO_2 at higher turnover rates than Rh/Al_2O_3.[35] The differences between single-crystals and supported catalysts remain largely unexplained and require rigorous characterization prior to detailed kinetic studies and mechanistic density functional theory (DFT) investigations.

Spectral features observed in CO probe-molecule IR spectra of Rh supported on Al_2O_3 vary with Rh weight loading. Rh weight loadings of ~2% or less display vibrational bands at approximately 2020 and 2090 cm^{-1} that do not vary in frequency with CO coverage.[36,37] These IR bands correspond to a Rh gem-dicarbonyl species, $Rh(CO)_2$, formed by coadsorbed CO* on atomically dispersed Rh (*i.e.,* single-atom Rh sites). Vibrational bands at 1800−1950 and 2045−2070 cm^{-1} are present at high CO* coverage on larger (>4 wt %) Rh loadings, corresponding to Rh particles, and these bands approach frequencies observed for CO* on Rh(111), indicating the formation of larger Rh nanoparticles with well-defined terraces, as subsequently confirmed by X-ray diffraction.[36] Our prior work showed a mixture of atomically dispersed Rh and Rh nanoparticles on both 0.5 wt % and 5 wt % $Rh/\gamma\text{-}Al_2O_3$ samples,[2,11] similar to earlier work on 10 wt % Rh/Al_2O_3.[38] Kinetic and infrared studies suggest that surfaces of SiO_2-supported Rh are dominated by NO* in NO and CO mixtures (488 K, 34 mbar CO, 9.0 mbar NO).[39] Spectra for supported $Rh/\gamma\text{-}Al_2O_3$ in mixed NO/CO feeds show features at ~1740, ~1830, and ~1920 cm^{-1}, possibly attributable to anionic, neutral, and cationic Rh(NO) species,[40,41] although different spectral features have been identified on different samples in later studies.[3,42,43] Furthermore, the mixture of Rh nanoparticles and atomically dispersed Rh species complicates the interpretation of these prior FTIR data because the spectral features overlap, particularly as coverage varies. These spectral signatures for NO* on Rh particles have not been directly investigated in prior DFT studies that have examined single-crystal Rh surfaces or have omitted computationally expensive frequency calculations on large nanoparticle models.

https://doi.org/10.1021/acs.jpcc.1c05160
J. Phys. Chem. C XXXX, XXX, XXX−XXX

These characterization data indicate that single-crystal extended surfaces, large nanoparticles, and atomically dispersed Rh each have distinct adsorbate coverages and binding modes, but these complexities have seldom been considered in the development and use of DFT models of transition-metal catalysts. Recently, adsorptions on nanoparticle models have been studied with DFT and contrasted to single-crystal surfaces and have shown that nanoparticles can have higher coverages than surfaces, including supramonolayer coverages.[44−49] For example, our prior work shows that H*-covered 201-atom Ir and Pt particles saturate at 1.59 and 1.30 ML, respectively, during H_2 chemisorption,[47] which is typically used to probe the size of metal nanoparticles. Similarly, DFT calculations indicate that CO* saturates Ru_{201} particles at > 1 ML but Ru(0001) surfaces at 0.75 ML[45,48,49] and that S* saturates Ru, Re, and Pt nanoparticles at higher coverages than their corresponding (111) or (0001) surfaces.[44] Most relevantly, our prior work shows that Rh_{201} nanoparticles saturate at 1.38 ML NO*, while Rh(111) surfaces saturate at ∼0.7 ML.[46] These coverages affect relative reaction rates directly by altering reactant surface concentrations and indirectly by altering binding energies and barriers through coadsorbate interactions. Moreover, rates can depend sensitively on the density and flexibility of adlayers around MASI and transition states. For example, rates of CO* hydrogenation on Ru can increase by as much as 5× as the fractional coverage of vacant sites decreases from 10^{-2} to 10^{-4} ML because denser CO* adlayers on curved Ru nanoparticles solvate hydrogenation transition states better.[48] These small absolute changes in coverage may similarly affect the behavior of CO−NO reactions, and the differences in θ_{sat} between particles and single-crystal surfaces is key to understanding the aforementioned unexplained kinetic phenomena observed in this chemistry.

Additionally, prior DFT studies have shown that coadsorbate repulsion and dipole−dipole coupling cause vibrational frequencies to increase with increasing coverage for CO* on transition-metal surfaces.[15,50−53] Such peak shifts have been observed for atop CO* in prior studies using vibrational spectroscopy on both Rh single-crystal surfaces using high-resolution EELS (HREELS; 2015−2070 cm^{-1}, 90 K, 10^{-9} bar CO)[22] and reflection absorption IR spectroscopy (RAIRS) (2026−2080 cm^{-1}, 123 K, 10^{-8} to 10^{-6} Torr CO)[15] and supported Rh particles (2039−2067 cm^{-1} using FTIR spectroscopy; 323−573 K, 0.33 bar CO, 0.68 bar He).[54] However, the DFT studies examining this phenomenon only tested single-crystal surfaces and thus featured adlayers of atop-bound CO* that were not disrupted by the curvature of polycrystalline nanoparticles. It is unclear how the curvature of these nanoparticles alters the effect of coverage on vibrational frequencies.

An accurate model of the structure of Rh nanoparticles and their interactions with CO and NO at saturation is necessary for investigations of the NO_x reduction mechanism occurring on TWCs. Here, we use a combination of theory and experiment to characterize and compare a 10 wt % Rh/γ-Al_2O_3 sample with an average Rh particle size of ∼2.6 nm diameter, which is also devoid of atomically dispersed Rh species, to DFT-predicted behavior of Rh(111) surfaces and a 201-atom cubo-octahedral Rh nanoparticle. DFT calculations of Rh(111) surfaces show that they saturate at 0.56 and 0.67 ML for CO* and NO*, respectively, but that Rh_{201} particles saturate at 1.00−1.10 and 1.38 ML of CO* and NO*. CO and NO probe molecule FTIR spectra show dominant stretching frequencies of CO*- and NO*-covered particles at 2067 and 1685 cm^{-1}, which correspond to calculated frequencies for atop-bound CO* and of threefold-bound NO* on Rh particles. Notably, Rh(111) surfaces show a near-equal mix of atop-bound and threefold-bound CO* at saturation coverage, while particles prefer atop-bound CO*, which appear more intensely in the IR spectra of the 10 wt % Rh sample examined in this work. Similarly, DFT predicts that NO* adlayers contain exclusively threefold NO* on Rh(111) but that adlayers on Rh_{201} particles are mixed, which more closely matches FTIR data for NO* at saturation coverage on our model Rh nanoparticle catalyst. These changes in coverage and binding mode preferences arise because nanoparticles are curved and their surface metal−metal (M−M) bonds expand (up to 7%) during optimization, which cannot occur on Rh(111) surfaces. These two factors contribute to lateral adlayer relaxation, altering both the saturation coverages on these surfaces and their characteristic frequencies and binding energies. We also show that this M−M expansion red-shifts characteristic stretching frequencies of both NO* and CO* by reducing adlayer strain and strengthening surface-adsorbate bonds by artificially expanding Rh(111) surfaces. Lastly, we show that while coverage and dipole−dipole coupling effects increase vibrational frequencies for CO* and NO* on metal particles, these effects approach a saturation behavior caused by the disruption of the surfaces across corner and edge atoms, which weakens the effects of dipole−dipole coupling. Taken together, these data indicate that nanoparticle models and the high coverages they predict more closely match the behavior of supported Rh catalysts than single-crystal models.

2. MATERIALS AND METHODS

2.1. Computational Methods and Models. Periodic DFT calculations were completed using the Vienna ab initio simulation package (VASP)[55−58] in the computational catalysis interface (CCI).[59] The revised Perdew−Burke−Ernzerhof (RPBE) form of the generalized gradient approximation (GGA) was used for all calculations,[60,61] and plane waves were composed of projector augmented-waves (PAWs)[62,63] with an energy cutoff of 400 eV, unless otherwise noted. For comparison purposes, additional calculations were performed using the Perdew−Burke Ernzerhof (PBE),[61] Perdew−Wang 91 (PW91),[64] and Bayesian error estimation (BEEF)[65] GGA functionals with PAW plane wave basis sets and some calculations used the PW91 functional with ultrasoft pseudopotentials (USPP).[66,67] Structures were optimized using a multistep process implemented in the CCI. Wave functions were converged to within 10^{-4} eV in the first step with forces calculated using a fast Fourier transform (FFT) grid of 1.5× the plane wave cutoff. Wave functions were optimized in the second step within 10^{-6} eV and with an FFT grid 2× the plane wave cutoff. Structures were optimized such that forces on all atoms were <0.05 eV $Å^{-1}$ in both steps. Gas-phase species were modeled in 18 × 18 × 18 $Å^3$ unit cells surrounded by vacuum with spin polarization for species with partially occupied orbitals in their valence shells (*e.g.,* NO).

Two types of Rh models were used in this work: a periodic Rh(111) surface and a cubo-octahedral Rh_{201} nanoparticle. The 3 × 3 Rh(111) surface contained four layers, the bottom two of which were fixed in their bulk crystallographic positions during optimization, with a 10 Å vacuum above its top layer. Calculations on periodic Rh(111) surfaces used a Γ-centered 4

https://doi.org/10.1021/acs.jpcc.1c05160
J. Phys. Chem. C XXXX, XXX, XXX−XXX

× 4 × 1 K-point mesh.[68] After the two-step optimization, a single-point calculation using an 8 × 8 × 1 K-point mesh with the same electronic convergence criteria as the second step (wave functions vary $<10^{-6}$ eV, FFT grid 2× plane wave cutoff) was used to determine electronic energies on Rh surfaces.

The cubo-octahedral Rh nanoparticle model contained 201 Rh atoms (1.7 nm diameter) and was placed at the center of a 31 × 31 × 31 Å^3 unit cell surrounded by ∼15 Å vacuum on each side. The Rh nanoparticles each had eight (111) and six (100) facets exposed, identical to that used in prior studies of NO adsorption and reduction on Rh (Figure 1).[46] Similar

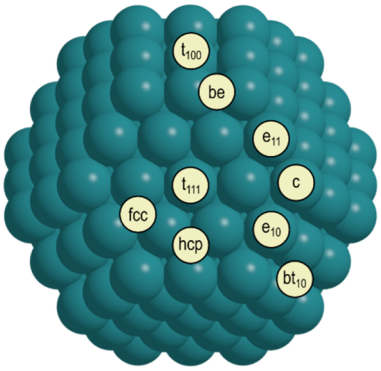

Figure 1. Distinct binding sites available on the Rh_{201} model used in this work. Terrace (t) sites have subscripts with their corresponding facets, edge sites can be between two (111) terraces (e_{11}) or between (111) and (100) terraces (e_{10}), and bridge sites can be on edges (be) or on the (100) terrace (bt_{10}).

nanoparticle structures were used to analyze high coverages during H_2 chemisorption on Ir and Pt,[47] C−C hydrogenolysis on Ir,[69] and CO hydrogenation on Ru.[48] On Rh nanoparticles, the Brillouin zone was sampled only at the Γ-point (a 1 × 1 × 1 mesh).

Adsorption on Rh surfaces and nanoparticles was analyzed similarly to prior work.[46,47] The NO* saturation coverages on the Rh(111) surface and a 201-atom Rh nanoparticle were previously found to be 0.67 and 1.38 ML, respectively.[46] We extend this work using CO as an adsorbate on the Rh surface and particle models to assess competitive adsorption in NO−CO reduction environments. On Rh(111), CO* coverage was varied between 0.11 and 1 ML (1−9 CO* adsorbates on this 3 × 3 surface model). At each coverage, multiple configurations were examined that varied the binding modes (*e.g.*, atop and threefold) and arrangements of CO*. A differential binding energy ($\Delta E_{\mathrm{diff},i}$) was calculated for each CO added to the surface

$$\Delta E_{\mathrm{diff},i} = E_{\mathrm{CO}^*,i} - E_{\mathrm{CO}^*,i-1} - E_{\mathrm{CO(g)}} \quad (4)$$

where $E_{\mathrm{CO}^*,i}$ is the energy of the most stable configuration with i CO* and $E_{\mathrm{CO(g)}}$ is the energy of gas-phase CO. Rh_{201} particles have 122 surface Rh atoms, and thus, it is impractical to consider singular sequential CO* adsorption events and to consider all arrangements of submonolayer CO* adlayers. As such, CO* were added to fill all locations of one unique binding mode on the Rh particle, consistent with prior work.[46,47] For example, CO* can be added to all atop positions on corner atoms of the Rh particle or to all bridge positions along the edge between two adjacent (111) terraces. These unique binding positions are shown in Figure 1. An "average differential" binding energy ($\Delta \bar{E}_{\mathrm{diff},i}$) is calculated for each unique site type that is filled at each subsequent CO* addition step

$$\Delta \bar{E}_{\mathrm{diff},i} = \frac{E_{\mathrm{CO}^*,i} - E_{\mathrm{CO}^*,i-x} - xE_{\mathrm{CO(g)}}}{x} \quad (5)$$

where x is the number of new CO* adsorbed.

Frequency calculations of optimized structures were used to determine zero-point vibrational energies (ZPVE) and rotational, translational, and vibrational enthalpies (H) and free energies (G) at 473 K based on formalisms from statistical mechanics (Section S1, Supporting Information).[70] Translation and rotation of adsorbates on surfaces were treated as frustrated motions and modeled as vibrations, while translation and rotation of gas-phase species were treated as ideal, and corresponding translational and rotational partition functions were used to calculate enthalpy

$$H = E_0 + \mathrm{ZPVE} + H_{\mathrm{vib}} + H_{\mathrm{rot}} + H_{\mathrm{trans}} \quad (6)$$

and free energy

$$G = E_0 + \mathrm{ZPVE} + G_{\mathrm{vib}} + G_{\mathrm{rot}} + G_{\mathrm{trans}} \quad (7)$$

Frequencies were calculated using a fixed displacement method (two displacements) in which all atoms in the Rh surface or Rh nanoparticle were frozen. Low-frequency modes (<60 cm^{-1}) were replaced with 60 cm^{-1}, consistent with prior work,[46,69,71] because low-frequency vibrations are inaccurately predicted by DFT, but their exclusion would exacerbate errors in computed adsorbate entropies. Calculated frequencies were scaled based on the gas-phase CO stretching frequency (2143 cm^{-1})[72] and the DFT-calculated gas-phase CO stretching frequency for each functional tested. For example, the calculated $CO_{(g)}$ frequency is 2102 cm^{-1} using the RPBE functional and PAW potentials, and therefore, all calculated frequencies using these methods were scaled by a factor of 1.019.

2.2. Experimental Methods. *2.2.1. Catalyst Synthesis.* Alumina (PURALOX TH100/150, Sasol) was dry-impregnated with an aqueous solution of $Rh(NO_3)_3$ (10 wt % Rh and 20−25% HNO_3, Alfa Aesar) to achieve an initial Rh loading of 6 wt %. The resulting material was dried at 373 K overnight, followed by dry impregnation with addition of $Rh(NO_3)_3$ solution to achieve a final Rh loading of 10 wt %. The material was then placed in an open dish (CoorsTek 60232) and set in a horizontally oriented tube furnace in a flow of air (0.025 L s^{-1}). The temperature was ramped at 0.25 K s^{-1} to 1073 K and held for 2 h in flowing air. Flow of air was then replaced by flow of N_2 (Airgas, 99.999%) for ∼600 s, followed by introduction of 1.25% H_2 in N_2 (Airgas). Flow of H_2 was maintained, while the temperature was held at 1073 K for an additional 2 h and then naturally cooled to 673 K. Flow of H_2 was discontinued, and the sample cooled to ambient temperature in flowing N_2.

2.2.2. Probe-Molecule FTIR Spectroscopy. The catalysts were loaded in a Harrick low-temperature reaction chamber mounted inside a Thermo Scientific Praying Mantis diffuse reflectance adapter set in a Nicolet iS10 FTIR spectrometer with a mercury cadmium telluride (MCT) detector. Mass flow controllers (Teledyne Hastings) were used to control the gas flow rates across the reactor bed. The catalysts were pretreated *in situ* for 0.5 h at 623 K in pure O_2 and subsequently in 10% H_2/Ar at 373 K. After *in situ* pretreatment, the samples were cooled to room temperature in flowing Ar, exposed to flowing

https://doi.org/10.1021/acs.jpcc.1c05160
J. Phys. Chem. C XXXX, XXX, XXX−XXX

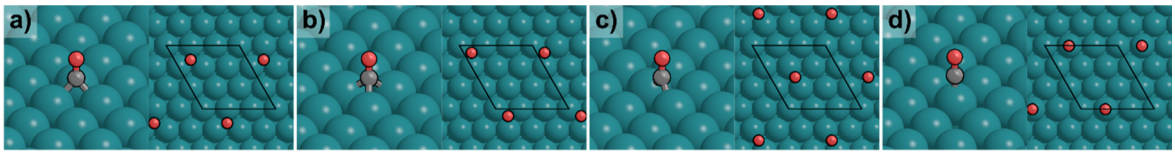

	3-fold hcp				3-fold fcc				bridge				atop			
	Binding E_0		ν_{CO}		Binding E_0		ν_{CO}		Binding E_0		ν_{CO}		Binding E_0		ν_{CO}	
RPBE	**−158**	*(0)*	**1749**	*1716*	**−154**	*(4)*	**1759**	*1726*	**−149**	*(8)*	**1827**	*1793*	**−157**	*(0)*	**2003**	*1966*
PBE	**−194**	*(0)*	**1749**	*1731*	**−189**	*(5)*	**1762**	*1744*	**−183**	*(11)*	**1829**	*1811*	**−184**	*(10)*	**2008**	*1988*
BEEF	**−165**	*(0)*	**1750**	*1732*	**−161**	*(4)*	**1757**	*1739*	**−157**	*(8)*	**1824**	*1806*	**−163**	*(1)*	**2000**	*1981*
PW91	**−190**	*(0)*	**1760**	*1744*	**−186**	*(4)*	**1769**	*1753*	**−180**	*(10)*	**1838**	*1822*	**−189**	*(9)*	**2014**	*1996*
PW/US	**−193**	*(0)*	**1772**	*1737*	**−189**	*(4)*	**1775**	*1741*	**−182**	*(12)*	**1845**	*1809*	**−180**	*(13)*	**2021**	*1981*

Figure 2. Single CO* bound (a) at a threefold hcp site, (b) at a threefold fcc site, (c) in a bridge position, and (d) atop on Rh(111). Binding energies (kJ mol^{-1}), relative energies (in parentheses, kJ mol^{-1}), and CO* stretching frequencies (ν_{CO}, cm^{-1}), both scaled (bold) and unadjusted (italicized), are shown for each configuration in four exchange−correlation functionals (RPBE, PBE, BEEF, and PW91) with PAW basis sets and with the PW91 functionals using USPP (PW/US).

1% CO or 0.5% NO in Ar at 1 bar until Rh sites were saturated while taking spectra with 12 scans and 0.482 cm^{-1} data spacing continuously until spectra remained unchanged, and then purged with Ar. TPD measurements were executed by heating the sample in Ar at a rate of 0.33 K s^{-1} until complete desorption of CO or NO was observed while taking spectra continuously during desorption every 10 s. Peak intensities and areas were integrated using Origin.

2.2.3. CO Chemisorption. Pulse chemisorption was performed in a Micromeritics chemisorption analyzer (AutoChem II 2920) loaded with 1 mg of total Rh diluted to 350 mg with plain γ-Al_2O_3 (PURALOX TH100/150, Sasol). Prior to chemisorption, the samples were treated at 673 K in flowing O_2 for 1 h, then at 623 K in 10% H_2/Ar for 1 h, and degassed under Ar at 623 K for 1 h (all gasses were sourced from Airgas and flowed at 3 L h^{-1}). Pulse chemisorption was performed at 303 K by dosing 0.5 mL of 10% CO/He over the catalyst every 180 s and analyzing the effluent with a thermal conductivity detector (TCD). The amount of chemisorbed CO was computed as the fractional area of the TCD signal consumed in each pulse relative to pulses with a stable area after saturation, assuming a constant dosage of 0.5 mL per pulse.

2.2.4. TEM Imaging of the 10 wt % Rh/γ-Al_2O_3 Sample. High-resolution scanning transmission electron microscopy (HRSTEM) was performed in a Thermo Fisher G2 200X operated at 200 kV. Samples were dispersed in isopropyl alcohol and drop-cast onto ultrathin lacey-carbon films supported on a Cu grid (Electron Microscopy Sciences). Prior to imaging, grids were loaded onto a single tilt holder and placed in a transmission electron microscopy (TEM) specimen holder vacuum station for 48 h to remove contamination. Imaging was performed under vacuum. To estimate the particle size distribution, particles were counted manually, and their areas were computed using ImageJ software. We report the number average particle diameter for reference, while the volume-area particle diameter was used to compute the Rh dispersion by assuming equal exposure of the (111), (110), and (100) facets (Section S3).[73]

2.2.5. NO Reduction Light-Off Experiment. "Light-off" experiments were performed to test the reactivity of the 10 wt % Rh/γ-Al_2O_3. The sample was heated in a glass tube reactor at a constant rate from ambient temperature to 673 K in reaction conditions to mimic engine startup. The catalysts were diluted with purified silicon dioxide (Sigma-Aldrich, CAS: 84878) to 2 mg Rh per gram of total material in a home-built, temperature-controlled reactor system with mass flow controllers (Teledyne Hastings) to precisely control CO, NO, H_2O, and Ar gas flow concentrations. After pretreatment identical to the CO FTIR characterization, the catalysts were heated at 300 K h^{-1} (5 K min^{-1}), while 250 sccm total flow rate of 5000 ppm CO and 1000 ppm NO in Ar flowed over a packed bed at 1 bar. Gas-phase product compositions were identified by flowing outlet effluent through a Thermo Scientific Antaris IGS 2-meter Gas Cell set in a Nicolet iS10 FTIR spectrometer with a MCT detector and using OMNIC series software to take five spectral scans every 10 s at high 0.5 resolution and 0.241 cm^{-1} data spacing. The reactants and products were calibrated with the TQ Analyst Pro Edition software to identify established spectral signatures of known mixtures of CO, NO, N_2O, NH_3, CO_2, and H_2O in Ar at set pressure and temperature.

3. RESULTS AND DISCUSSION

3.1. CO Binding on Rh(111). DFT predicts that CO* is equally stable at either an atop or threefold hcp site on Rh(111) at 0.11 ML (RPBE, PAW; Figure 2), partially consistent with surface science studies, which find that CO* binds atop on Rh(111) at low coverages.[15,74] We tested alternative DFT methods to assess the relative binding energies between different modes and methods at low coverage. PBE, PW91, BEEF, and RPBE functionals with PAW predict that a threefold hcp binding configuration is preferred over atop for CO* by 10, 9, 1, and 0 kJ mol^{-1}, respectively. PW91 with USPP (PW/US) predicted a preference for threefold over atop binding by 13 kJ mol^{-1}. Binding energies from DFT calculations are weakest for the RPBE and BEEF functionals with values of −158 and −165 kJ mol^{-1}, respectively, for the threefold hcp site (Figure 2). These functionals typically predict that adsorbates bind more weakly on metals than other GGA functionals.[75,76] PBE and PW91, in contrast, predict binding strengths of −194 and −190 kJ mol^{-1}, respectively, similar to previous DFT investigations of CO binding on Rh(111).[77] Experimental ultrahigh vacuum (UHV) thermal desorption mass spectroscopy studies have estimated CO binding energy (ΔE) on the order of −130 to −150 kJ mol^{-1}, depending on initial CO* coverage and corresponding temperature at which CO* desorbs.[15,17,22,78] These data indicate that RPBE and BEEF best predict the binding behavior of CO on Rh(111).

DFT-calculated vibrational frequencies vary from ∼1750 to ∼2000 cm^{-1} as the binding mode shifts from threefold (three

https://doi.org/10.1021/acs.jpcc.1c05160
J. Phys. Chem. C XXXX, XXX, XXX−XXX

C−M bonds) to atop (a single C−M bond) for all functionals. Surface science studies using HREELS[22] (90 K) and RAIRS[15] (123 K) of CO* on Rh(111) do not observe any bands below 1900 cm^{-1} until CO* coverage exceeds 0.5 ML, which indicates a lack of significant CO* coverage in bridge or threefold positions. Above 0.5 ML CO*, a feature near 1825 cm^{-1} appears in these HREELS and RAIRS data on Rh(111), suggesting that some CO* is bridge-bound at high CO* coverages based on the DFT-calculated frequencies in Figure 2;[15,22] however, these frequencies are computed at 0.11 ML, not at elevated CO* coverages, and CO* stretching frequencies may change with coverage. The calculated frequency for threefold CO* at 0.11 ML on Rh(111) (1749 and 1759 cm^{-1}) is in close agreement with the observed frequency for a single CO* bound threefold on a Rh_4 cluster (1731 cm^{-1}),[79] despite the structural differences between small clusters and extended surfaces.

As CO* coverage increases on Rh(111) surfaces, DFT predicts that exclusively atop modes become slightly preferred at 0.22−0.33 ML (Figure 3a). Mixed binding modes (atop and threefold) are preferred from 0.44 to 0.78 ML, above which all CO* prefer to bind to threefold fcc sites. These results are somewhat consistent with surface science experiments, which indicate that CO forms adlayers of atop-bound CO* at low coverage but shifts to adlayers with mixed binding modes at higher coverages.[15,80−82] The formation of threefold-dominated adlayers at high coverages is not observed because such coverages are not accessible during surface science studies. These calculations predict that differential adsorption energies (E_0) become positive, indicating unfavorable adsorption at coverages above 0.78 ML, which appears to match maximum possible CO saturation coverages observed in surface science experiments (~0.75−0.78 ML, 90−123 K).[15,80,81] Notably, the (2 × 2)-3CO organization observed at 0.75 ML using low-energy electron diffraction (LEED)[80] cannot be replicated on the 3 × 3 surface model used in this work. Our calculations find ΔG_{diff} values remain negative up to 0.78 ML (ΔG_{diff} = −24 kJ mol^{-1}) and become positive at 0.89 ML (ΔG_{diff} = +201 kJ mol^{-1}) at 95 K. These data show general agreement between the DFT methods employed here and surface science observations for both the adsorption energies, free energies, and binding modes of CO*, with the exception of the 0.11 ML binding mode. At the catalytically relevant temperature of 473 K, however, differential standard state adsorption free energies (ΔG_{diff}, 473 K, 1 bar) only remain negative up to 0.56 ML CO* (ΔG_{diff} = −22 kJ mol^{-1}); the adsorption of an additional CO*, yielding a coverage of 0.67 ML, has a ΔG_{diff} of +3 kJ mol^{-1}, indicating that CO coverage does not reach 0.67 ML on Rh(111) under these conditions. This saturation coverage is lower than that observed in surface science experiments because entropic losses from adsorption counteract enthalpic benefits at higher temperatures (473 K) more than at the low temperatures of these surface science experiments (90−123 K).

We calculate the vibrational frequencies of CO* on Rh(111), including the dipole moment, from which the relative intensities of each vibrational mode and frequency can be estimated. Previous UHV LEED,[17,22,78] reflection absorption infrared spectroscopy (RAIRS),[15] and EELS[22] studies of CO* on the Rh(111) surface indicate that the stretching frequency of CO* bound atop to Rh(111) increases (blueshifts) as coverage increases, in conjunction with the appearance of a peak associated with threefold CO*.

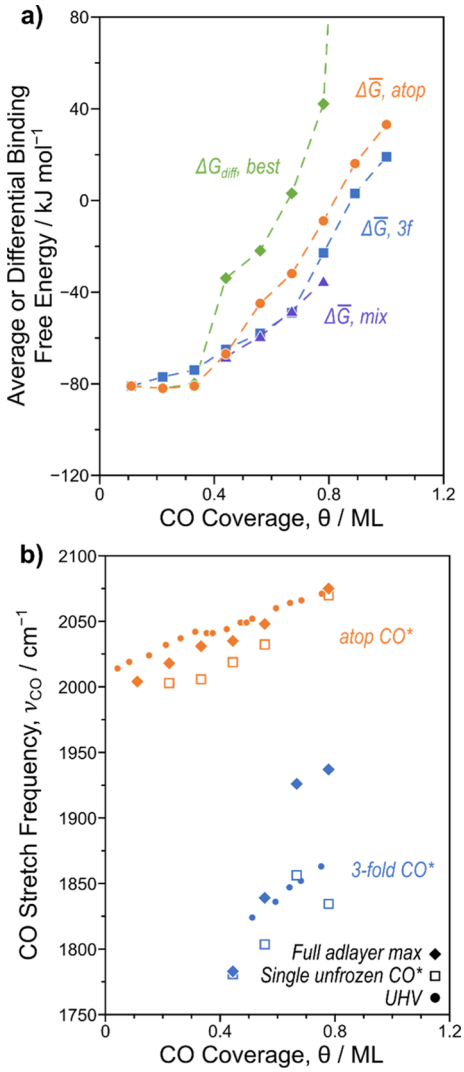

Figure 3. (a) Average binding free energies (473 K, 1 bar) on Rh(111) as a function of coverage of CO on Rh(111) surfaces in atop (●, orange), threefold (■, blue), and a mixture of binding modes (▲, purple) and the differential binding free energy (ΔG_{diff}; 473 K, 1 bar) for the best configuration (◆, green). (b) Maximum calculated CO* stretching frequency for the best configuration with the entire adlayer permitted to move (◆) and with only one CO* permitted to move (■, hollow) from 0 to 0.78 ML CO* for atop (orange) and threefold (blue) binding modes (data up to 1.0 ML are shown in Figure S4, Supporting Information). Small dots in (b) show experimental HREELS data (90 K) from Linke *et al.*[22]

Moreover, CO* stretching frequencies are dipole-coupled such that CO* bound at identical sites and on flat surfaces vibrate in phase, and the intensity of this vibration is stronger than out-of-phase vibrations.[15,22] Our calculations indicate that CO* frequencies on Rh(111) surfaces increase with coverage, and as coverage increases, the range of frequencies among CO* stretches increases (Figure S4, Supporting Information). Predicted intensities based on dipole-moment calculations, however, indicate that in-phase vibrations (which have higher frequencies) disproportionately contribute to the observed frequencies for CO* on Rh(111) (Tables S1−S3, Supporting Information). Therefore, we emphasize the highest calculated frequencies in the adlayer for atop CO* and threefold CO*, particularly for the most stable configuration at all coverages. Because only atop CO* is observed below 0.5 ML

https://doi.org/10.1021/acs.jpcc.1c05160
J. Phys. Chem. C XXXX, XXX, XXX−XXX

experimentally, we focus on atop CO* at 0.11 ML despite its nearly identical energy to CO* at a threefold hcp site. The maximum stretching frequency for a CO* bound atop is 2004 cm^{-1} at 0.11 ML, shifting to 2069 cm^{-1} at 0.56 ML (the highest mixed-mode coverage possible at 473 K) and further increasing to 2126 cm^{-1} at 1.0 ML when all CO* are bound atop (a coverage and configuration that is only possible in DFT calculations, although unfavorable). Similarly, the maximum frequency for CO* bound threefold increases from 1749 cm^{-1} at 0.11 ML to 1899 cm^{-1} at 0.56 ML and further to 1976 cm^{-1} at 1.0 ML when all CO* is bound threefold; however, these uniform binding modes do not persist at all coverages. These calculations illustrate the possible changes in frequencies (124 and 237 cm^{-1} for CO* in atop and threefold modes) when CO* reaches coverages above those that are realistically possible and when occupying only specific binding modes—a degree of control only possible in DFT calculations. When CO* is permitted to occupy mixed binding modes (which occurs preferentially above 0.33 ML), similar blue-shifting of peaks is observed, albeit for separate atop and threefold CO* vibrations (Figure 3b). The maximum frequencies for atop and threefold binding modes at each coverage correspond closely to those observed using EELS as CO* coverage on Rh(111) increases.[22] We also calculated frequencies with only one atop-bound or threefold-bound CO* permitted to vibrate at all coverages to estimate the role of dipole−dipole coupling shifting frequencies for in-phase vibrations. These frequencies similarly increase with CO* coverage but are lower than the frequencies for in-phase vibrations of the full adlayer (Figure 3b). Therefore, when additional adsorbates are present, calculating the C−O stretching frequency separates the effects of coverage from those of dipole−dipole coupling. The trend in stretching frequency for atop CO* as a function of coverage on Rh(111) agrees very well between experiment (2015 to 2070 cm^{-1}) and theory (2004 to 2069 cm^{-1} for the full vibrating adlayer). While these Rh(111) calculations match observations for coverage-dependent binding energies and vibrational frequencies from surface science studies, they are idealized models; realistic supported catalysts are polycrystalline and expose sites with varying coordination, such as corner and edge atoms.

3.2. HRSTEM Particle Size Assessment of the 10 wt % Rh/γ-Al_2O_3 Sample. Small Pt-group metal particles can restructure and redisperse when interacting with probe molecules such as CO and NO.[37,83−85] These metal clusters can fragment into single atoms because the binding energy between the probe molecule and dispersed species coordinated to the support is greater than the binding energy between adjacent Rh atoms within nanoparticles.[85−87] Small Rh particles (<2 nm diameter) interacting with CO in particular separate into atomically dispersed $Rh(CO)_2$ species, where the oxidative fragmentation process is accompanied by the reduction of protons on the oxide support.[88,89] Therefore, cycling the catalyst through harsh reducing pretreatment conditions to form large Rh particles and stripping the oxide surface of hydroxyl ligands that facilitate mobility is key to obtaining a catalyst with exclusively Rh nanoparticles and without atomically dispersed Rh. Notably, while prior investigations have analyzed supported Rh clusters experimentally,[37−39] few have rigorously insured against the existence of atomically dispersed species and compared these samples to DFT-calculated CO* and NO* frequencies.[54,90,91] Removal of the atomically dispersed Rh species is critical for such analysis because the CO* stretching bands of $Rh(CO)_2$ partially overlap with CO* on Rh nanoparticles, particularly because of coverage-dependent vibrational frequency shifts for atop CO* on Rh nanoparticles. As such, the sample used to characterize CO and NO binding to γ-Al_2O_3-supported Rh nanoparticles required a high weight loading (10 wt %) and high-temperature pretreatment and ageing. The combination of elevated temperature, high mass loading, and reducing conditions was used to avoid the formation of atomically dispersed Rh species.

HRSTEM was used to quantify Rh particle sizes in the 10 wt % Rh/γ-Al_2O_3 sample and examine particle geometries. A count of 250 particles in the peripheral regions of the image, where particles are discernible, indicates that the number average particle diameter is 2.6 nm ± 1.1 nm (Figure 4; see Section S3 for details of particle size estimations). Notably, particles of this size exhibit curvature which induces differences in the characteristics of adsorbates as compared to single-crystal surfaces because of differing surface structures, intermolecular interactions among adsorbates, and surface relaxation, among others. Therefore, we employ CO as a probe molecule to characterize these samples and compare the results to previous analyses on single-crystal Rh surfaces and DFT calculations on both curved nanoparticle and (111) surface models.

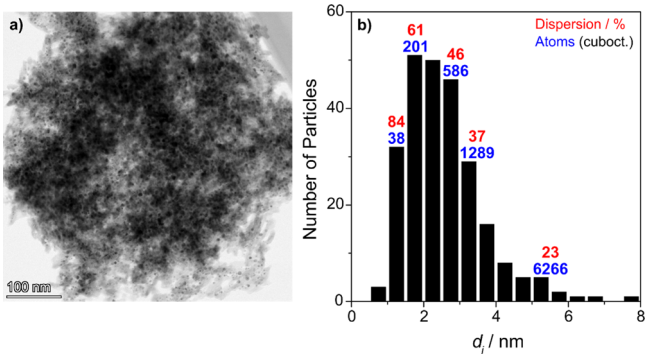

Figure 4. (a) Bright field-HRSTEM (BF-HRSTEM, 185k× magnification) of 10 wt % Rh/γ-Al_2O_3 and (b) corresponding particle size distribution computed from a count of 250 particles in the peripheral regions of the image. Values of dispersions (%) and number of atoms as a function of particle size are presented for cubo-octahedral particle models for comparison.

3.3. Characterization of γ-Al_2O_3-Supported Rh Nanoparticles Using Probe Molecule CO FTIR Spectroscopy. Figure 5 provides spectral signatures of CO* on 10 wt % Rh/γ-Al_2O_3 after the sample had been saturated with CO* while Ar flowed over the catalyst as temperature increased 0.33 K s^{-1}. The absence of bands at 2090 and 2020 cm^{-1} (the symmetric and asymmetric stretches associated with $Rh(CO)_2$)[37,38,92] indicates that no atomically dispersed Rh is present. Instead, stretches associated solely with CO* on Rh nanoparticle surfaces are found at saturation coverage and room temperature, as indicated by features at 2067, 1955, and 1865 cm^{-1}. The 2067 cm^{-1} feature is assigned to CO* at atop adsorption sites, while the 1955 and 1865 cm^{-1} stretches have been previously assigned to CO* on bridge sites on (100) facets, and CO* at threefold sites on (111)-like facets, respectively.[22,93] Variations in the frequency and relative intensity of CO* bands on Rh nanoparticles as a function of temperature

https://doi.org/10.1021/acs.jpcc.1c05160
J. Phys. Chem. C XXXX, XXX, XXX−XXX

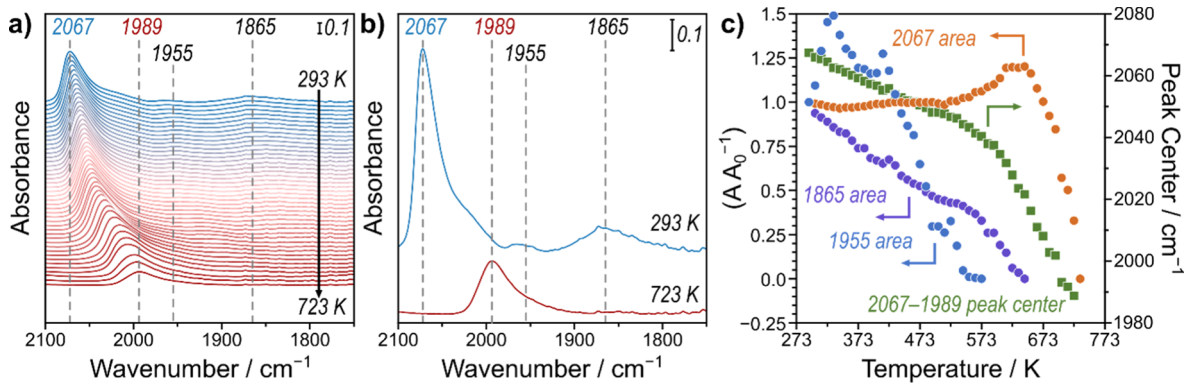

Figure 5. IR spectra of 10 wt % Rh/γ-Al_2O_3 (a) taken every 10 K as the temperature increases 0.33 K s^{-1} from 293 to 723 K after the sample is fully saturated with CO and (b) shown in detail at 293 and 723 K, identifying linear-bound CO* (2067−1989 cm^{-1}), bridge-bound CO* (1955 cm^{-1}), and threefold-bound CO* (1865 cm^{-1}). (c) Change in the relative peak area ($A{\cdot}A_0^{-1}$, ●) for the 2067−1989 cm^{-1} (orange), 1955 cm^{-1} (blue), and 1865 cm^{-1} (purple) peaks and the shift in the peak center for the 2067−1989 cm^{-1} peak (green, ■) as a function of temperature.

(and thus coverage) shown in Figure 5 provide comparisons to previous similar measurements on Rh(111),[17,22] Rh(100),[93,94] and stepped Rh(553) surfaces.[21]

The vibrational frequencies for all three CO* species redshift with increasing temperature during TPD, with disappearance of the bands at different temperatures: threefold-bound CO* (1865 cm^{-1} at saturation coverage) disappears by ∼623 K, atop-bound CO* (2067 cm^{-1} at saturation coverage) disappears by 723 K, and bridge-bound CO* (1955 cm^{-1} at saturation coverage) disappears by ∼573 K. Disappearance of the bridge and threefold CO* prior to atop CO* is consistent with the preference of CO* for atop adsorption at lower coverages and rapid CO* diffusion between atop and threefold or bridge sites. The relatively high temperature at which atop CO* are observed in these studies, as compared to previous analysis on single crystals, likely stems from the slower ramp rate during the TPD in this work (0.33 K s^{-1} compared to ∼5 K s^{-1} common in single-crystal studies) and the existence of undercoordinated surface sites on small Rh nanoparticles that bind CO* strongly.[95] We note that the *in situ* cell used here exhibits temperature gradients,[96] although we calibrated the surface temperature using an optical pyrometer and in-bed thermocouple.

The atop CO* frequency redshifts from 2067 cm^{-1} at saturation coverage to 1989 cm^{-1} at the lowest observed coverage, the latter of which matches closely to atop monocarbonyl stretches on small Rh clusters (1959−1962 cm^{-1} on $Rh_n(CO)$, n = 5−15).[79] The atop CO* stretching frequency at saturation coverage observed here is consistent with measurements on single-crystal surfaces at ∼300 K (2064−2070 cm^{-1} depending on surface facet), suggesting a similar primary normal mode of the coupled vibrating CO* species. The shift in CO* frequency observed during TPD from Rh nanoparticles shows a ∼78 cm^{-1} total shift to a final frequency of 1989 cm^{-1}, larger than the span of atop CO* vibrational frequencies observed on the single-crystal surfaces (∼50−55 cm^{-1}), which exhibit atop CO* frequencies >2000 cm^{-1} at the lowest coverage. The distinct behavior of atop CO* on Rh particles (frequency span at changing coverage and frequency at lowest coverage) suggests that there exist highly undercoordinated sites, which do not exist on Rh single crystals, and further that dipole−dipole coupling occurs between CO* on the various adsorption sites on Rh particles despite their curvature and, therefore, the imperfect alignment of CO*.

The feature assigned to threefold CO*—1865 cm^{-1} at saturation coverage—is consistent with the observed frequency of threefold CO* at saturation coverage on Rh(111) (1861 cm^{-1}).[22] Similarly, the frequency of the band assigned at 1955 cm^{-1} to bridge-bound CO* observed at saturation coverage on Rh nanoparticles is consistent with similar observations on (100) and (553) surfaces of a band at ∼1940 cm^{-1}. The ∼1955 cm^{-1} peak associated with bridge-bound CO* redshifts by ∼15 cm^{-1} during the TPD to 1938 cm^{-1} at 563 K, indicating that the CO* frequency and intensity decrease with decreasing CO* coverage similarly to atop CO* but with smaller changes in the frequency.

The change in relative CO* band intensity during the TPD also provides a basis for comparing the behavior of CO* adlayers on Rh nanoparticles to single-crystal surfaces (Figure 5c). The atop CO* relative band intensity stays consistent up to 550 K, even with decreasing vibrational frequency, and then increases in intensity by ∼20% at 650 K, followed by a sharp decrease. The increase in atop CO* band intensity occurs after the bridge CO* band has depleted and is accompanied by a sharp decrease in the threefold CO* band intensity, which suggests that CO* only occupies bridge and threefold sites at very high coverages and that any vacancies in atop sites are readily filled by the diffusion of CO* from bridge and threefold sites. The steady intensity of the atop CO* band up to 550 K, even with a shift in vibrational frequency, could be explained by an increasing extinction coefficient of the primary normal mode at lower coverage.[23] Qualitatively, these results are consistent with previous experiments on single-crystal surfaces; however, when CO* coverage on supported Rh particles decreases with rising temperature, the absolute value of the increase in the intensity of the atop CO* band is less than what is observed for Rh(111) surfaces. On Rh(111), the absolute value of the intensity change between 0.75 and 0.5 ML for the atop CO* band is >50% of the maximum intensity at 0.5 ML. While we do not have a direct measure of CO* coverage during TPD from Rh nanoparticles, the trend in atop, bridge, and threefold CO* intensities during the TPD indicates differences in relative site preference on single-crystal and Rh nanoparticle surfaces. The Rh(100) and Rh(111) studies suggest significant changes in the preferred binding modes of CO* with coverage, while smaller changes are observed for Rh

https://doi.org/10.1021/acs.jpcc.1c05160
J. Phys. Chem. C XXXX, XXX, XXX−XXX

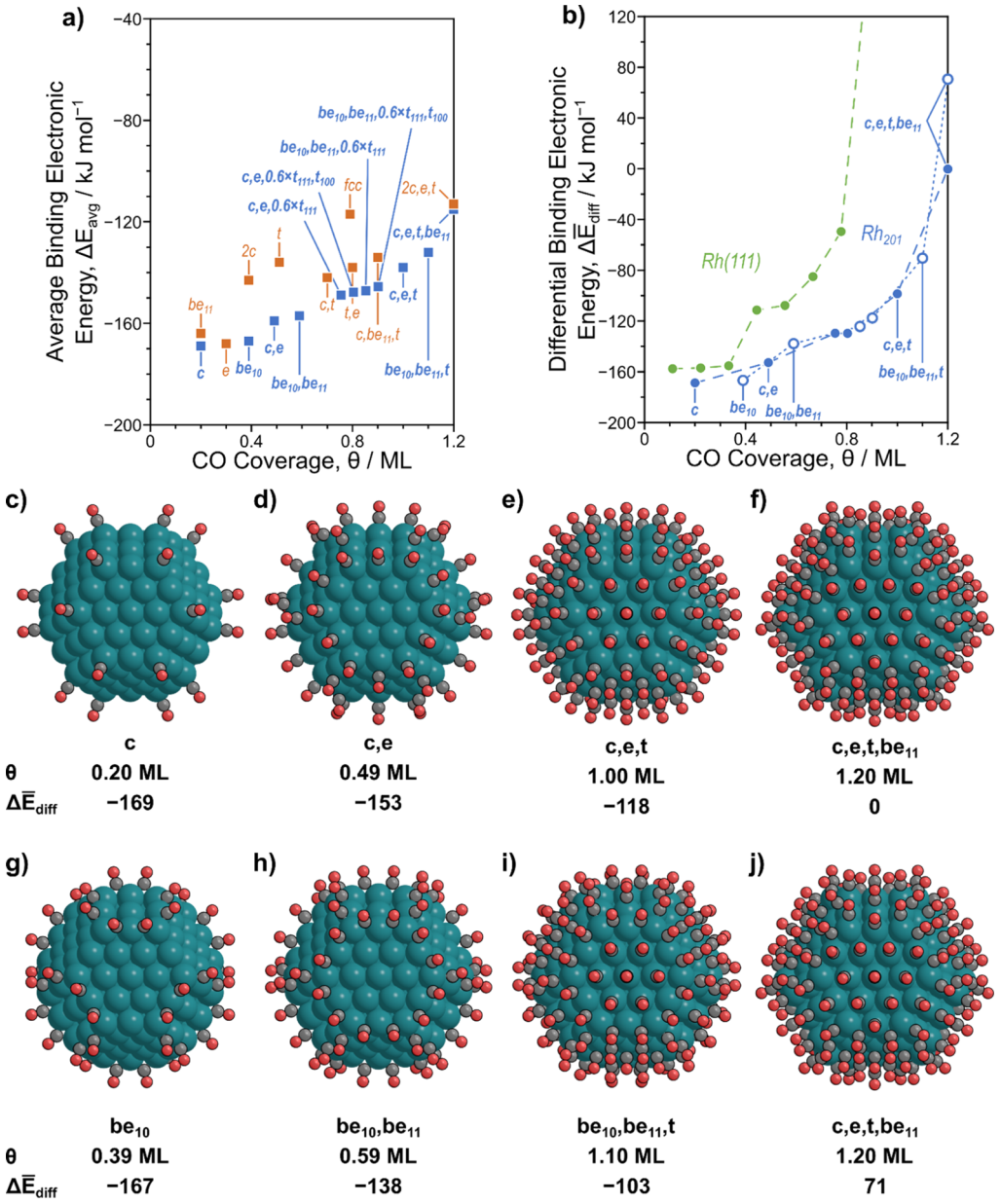

Figure 6. (a) Overall average CO binding energies on the Rh_{201} nanoparticle (■) with the most likely configurations to fill the particle (blue) and all other configurations tested that were optimized without adlayer reorganization (orange). (b) Average differential (●) electronic binding energies for CO as a function of coverage on the Rh(111) surface (green) and on the Rh_{201} particle model for the path leading to the c,e,t-covered particle (blue, filled with dashed lines) and leading to the be_{10},be_{11},t-covered particle (blue, hollow with dotted lines). The configurations of CO* for only atop filling at (c) 0.20, (d) 0.49, (e) 1.00, and (f) 1.20 ML on the Rh_{201} particle and the configurations with CO* bound on bridge-edge sites during filling at (g) 0.39, (h) 0.59, (i) 1.10, and (j) 1.20 ML.

nanoparticles at higher coverage. This is interpreted from the 20% increase in atop CO* band intensity from the maximum CO* coverage at 293 K and to the maximum intensity during the TPD at 653 K in contrast to 40 and 50% changes for CO* adlayers on Rh(100) and Rh(111),[22] respectively.

Direct comparisons between the IR signatures of CO* on Rh nanoparticles from a model Rh/γ-Al_2O_3 catalyst devoid of atomically dispersed Rh and Rh single crystals show distinct behavior of CO* adlayers on Rh nanoparticles. CO* adlayers on Rh nanoparticles contain a wider variety of surface site coordination environments (from the larger CO* frequency span with changing coverage) and decreased magnitude of site preference at saturation coverage (from the smaller change in atop CO* band intensity *vs* coverage) as compared to Rh single-crystal surfaces.

3.4. CO Binding to Rh Nanoparticles. Cubo-octahedral cluster models have been used to address the effects of coverage and particle size on metal-catalyzed NO−H_2,[46] CO−H_2,[48] and alkane−H_2 reactions,[69] as well as H_2[47] and S* (from H_2S) chemisorption.[44] These prior studies all demonstrate that the saturation coverages predicted for the abundant surface intermediates (NO*, CO*, H*, and S*) are higher for particle models than for periodic single-crystal surfaces. These adsorbates bind more strongly to particles at high coverages than to flat surfaces because particles allow the metal catalyst to expand as coverage increases and allow the surface adlayer to laterally relax to minimize coadsorbate repulsions. Here, we

https://doi.org/10.1021/acs.jpcc.1c05160
J. Phys. Chem. C XXXX, XXX, XXX−XXX

examine CO* adsorption on 201-atom Rh clusters that primarily expose its most stable facets—(111) and (100)[97]—and the CO* adsorption energies and vibrational frequencies on these particle models are contrasted to those calculated on Rh(111) surfaces.

CO* can bind atop metal atoms with six distinct environments and varying coordination numbers (CNs) on the Rh_{201} particle (Figure 1): corner atoms (c, CN = 6), edge atoms (e_{10} and e_{11}, CN = 7), (100) terrace atoms (t_{100}, CN = 8), and at two positions on the (111) terrace (t_{111}, CN = 9). The CO* binding energies for adsorption to these six atoms become more exothermic as the CN of the metal atom decreases from −146 kJ mol^{-1} on the central (111) terrace atom to −172 kJ mol^{-1} on a corner atom (Figures S5−S6, Supporting Information), as expected from bond-order conservation models[98] and prior CO adsorption studies.[49,99,100] CO* can also bind to six distinct threefold sites with binding energies ranging from −163 to −147 kJ mol^{-1} with a much weaker dependence on the average CN of the metal atom ensemble (Figure S6, Supporting Information). CO* binds most strongly to bridging sites on the edge between adjacent (111) and (100) terraces at these low coverages with an adsorption energy of −176 kJ mol^{-1}, almost 20 kJ mol^{-1} more negative than on any site of the Rh(111) surface at low coverage.

Multiple CO* were added to all sites for a specific binding mode on the Rh_{201} model (*e.g.*, atop on all corner atoms and atop on all (111) and (100) terrace atoms) to simulate filling of the surface, as described in Section 2.1 and shown in Figure 6. The average differential binding energies ($\Delta\bar{E}_{diff}$) for each addition describe the binding energies of added CO* between adlayers. Computing the vibrational entropies of all CO* on these models at high coverage is computationally intractable; therefore, we estimate a $\Delta\bar{E}_{diff}$ at which surfaces saturate with CO* by assuming that entropy loss upon adsorption to Rh particles is similar to that for adsorption on Rh(111) surfaces. Entropy losses near saturation coverages on Rh(111) surfaces suggest that a ΔE_{diff} near −85 kJ mol^{-1} will result in a ΔG_{diff} near 0. Filling calculations on Rh_{201} suggest that CO* first binds to corner sites ($\Delta\bar{E}_{diff}$ = −169 kJ mol^{-1}; Figure 6c), on edge sites ($\Delta\bar{E}_{diff}$ = −167 kJ mol^{-1}), or be_{10} sites ($\Delta\bar{E}_{diff}$ = −167 kJ mol^{-1}; Figure 6g) as all have binding energies indistinguishable to DFT methods. Following adsorption in one of these motifs, CO* will continue to adsorb to these undercoordinated sites, with the most likely being an arrangement in which CO* is bound atop to all corner and edge atoms (0.49 ML, Figure 6d), or at a slightly higher coverage (0.59 ML, Figure 6h) in which CO* bind to bridge sites between all corner and edge atoms. Once these undercoordinated sites are occupied, terrace sites fill with atop CO*, added here in three stages, first covering part of the (111) terraces, then the (100) terraces, and finally filling the remainder of the (111) terrace (Figures S8−S9, Supporting Information). The final structures have coverages of 1.00 ML with a final $\Delta\bar{E}_{diff}$ of −99 kJ mol^{-1} (−118 kJ mol^{-1} for all terrace sites on average; Figure 6e) or 1.10 ML with a final $\Delta\bar{E}_{diff}$ of −70 kJ mol^{-1} (−103 kJ mol^{-1} for all terrace sites on average; Figure 6i). These final binding energies bracket the critical $\Delta\bar{E}_{diff}$ (−85 kJ mol^{-1}) estimated from the entropy losses on the Rh(111) surface. Adsorption above these 1.00 ML or 1.10 ML configurations (*e.g.*, to form Figure 6f from 6e) occurs with a much higher $\Delta\bar{E}_{diff}$ (≥0 kJ mol^{-1}). In both the 1.00 and 1.10 ML adlayers, the (111) terraces of the particle are occupied by atop CO*, in contrast to high coverage calculations on Rh(111) single-crystal surfaces where a mixture of CO* bound to threefold and atop sites is observed. CO* binding to fcc modes on particles results in significantly higher binding energies than atop modes at comparable coverages (Figure 6a). This is consistent with the experimental comparison discussed above, where Rh nanoparticles exhibited reduced preference for threefold sites at high coverage as compared to Rh single crystals, although the band at ∼1865 cm^{-1} indicates that some CO* is bound threefold. These results suggest that on larger Rh nanoparticles, which certainly exist within the particle size distribution of the experimentally examined system, CO* in the center of (111) terraces may bind threefold similarly to flat Rh(111) surfaces, but that atop modes are preferred near edges and corners because particle curvature relieves the adlayer strain that encourages threefold binding. Based on these data, CO* saturates Rh_{201} nanoparticles at coverages near 1.00 ML, far above those predicted on Rh(111) surfaces (0.56 ML) and consistent with conclusions of prior studies of NO* on Rh,[46] H* on Ir and Pt,[47] CO* on Ru,[48,49] and S* on Pt, Ru, and Re particles.[44]

CO pulse chemisorption measurements,[101] in combination with HRSTEM images, were used to assess CO* saturation coverage on Rh particles in the 10 wt % Rh/γ-Al_2O_3 sample. Chemisorption quantified the CO uptake on the 10 wt % Rh/γ-Al_2O_3 sample, from which saturation coverage was obtained by comparison to the dispersion estimated from HRSTEM measurements. Hydrogen chemisorption is often employed for estimating dispersion by assuming one H* per Rh surface atom, but comparisons of hydrogen chemisorption with extended X-ray absorption fine structure (EXAFS)[102] and STEM[103] have indicated that the $H/Rh_{surface}$ stoichiometry can exceed unity for small Rh particles (<1 nm up to 5 nm)[102,103] and varies with particle size, similar to DFT studies showing similar results for small Ir and Pt particles.[47] Therefore, hydrogen chemisorption is an unreliable technique for estimating dispersion in nonuniform particle systems; instead, we rely on HRSTEM to assess the particle size distribution in the 10 wt % Rh sample.

Because of the high Rh weight loading of the sample, a particle count was only feasible for the peripheral regions of the imaged catalyst particle (Figure 4). A count of 250 particles yielded a number average particle diameter of 2.6 nm and dispersion of 31%. During pulse chemisorption at 303 K, the ratio of chemisorbed CO* to Rh atoms in the sample was 0.26, suggesting a CO* coverage of 0.84 ML. The precise dispersion is very sensitive to the particles imaged—for example, the addition of two 9 nm particles to a count of 250 particles, which could be easily obscured in the central region of the HRSTEM image, lowers the dispersion from 31 to 27% and raises the calculated CO* coverage to 0.95 ML. Similarly, counts of 37−150 particles in separate regions of the image yielded dispersions between 36 and 26%. Dispersions in this range (26−36%) would place the CO* saturation coverage between 0.72 ML—only slightly higher than an expected value for extended Rh surfaces[17]—and 1.0 ML, similar to the values suggested by DFT calculations on the Rh_{201} particle models in this work. In the absence of conclusive experimental methods for estimating saturation coverage of catalysts with nonuniform particle sizes, we propose the tandem use of DFT particle models and FTIR spectroscopy to predict adsorbate behavior on particle surfaces.

https://doi.org/10.1021/acs.jpcc.1c05160
J. Phys. Chem. C XXXX, XXX, XXX−XXX

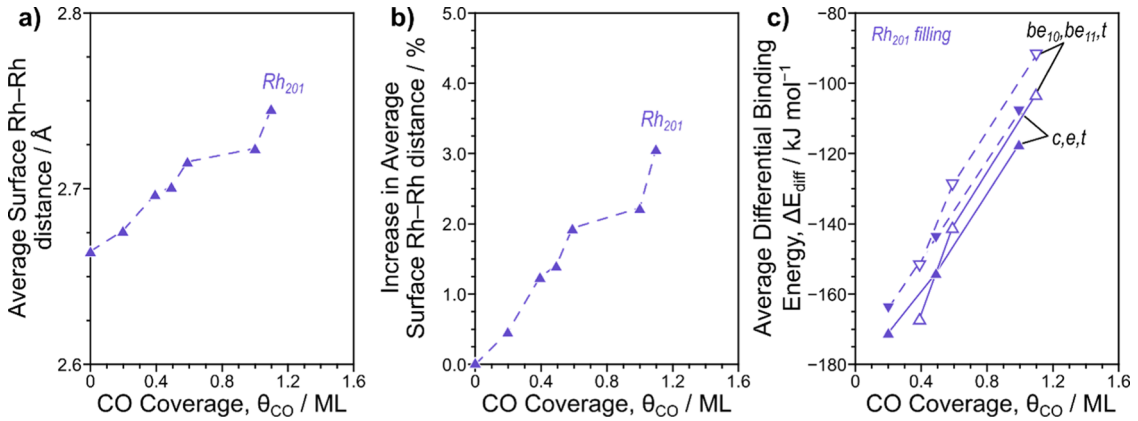

Figure 7. (a) Absolute values of and (b) percent increase in average length of Rh−Rh bonds on the surface of Rh_{201} (▲, purple) with increasing CO* coverage. (c) Average differential binding energies to fill the c,e,t sites (filled) and be_{10},be_{11},t sites (hollow) with the atoms of the underlying particle permitted to relax (▲, solid lines) and frozen in their original positions (▼, dashed lines).

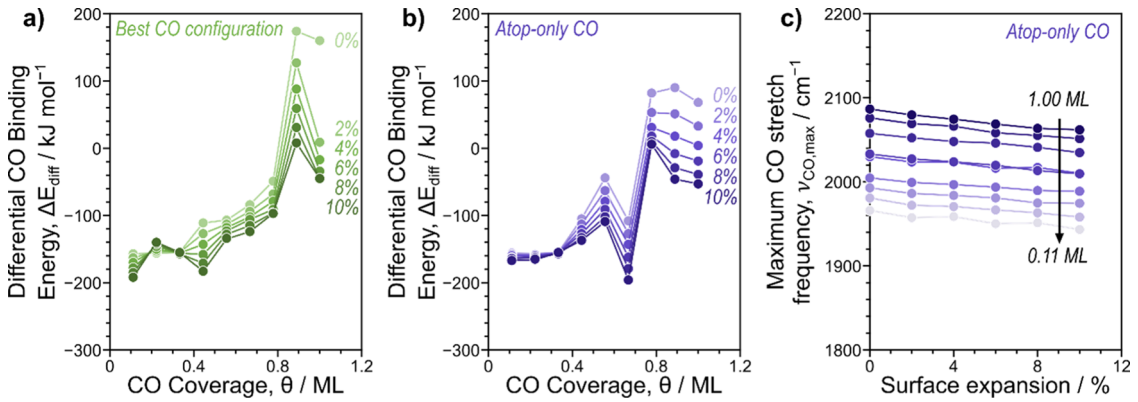

Figure 8. Differential CO* binding energies (ΔE_{diff}) on the Rh(111) surface as the unit cell was expanded 0−10% in 2% increments (light to dark with increasing expansion) for (a) the most stable CO* configuration overall and (b) the most stable configuration where all CO* are bound atop. (c) Highest calculated frequency for the atop-only configurations shown in (b) from 0.11 ML (light purple) to 1.0 ML (dark purple) as the unit cell expands.

The higher-saturation CO* coverages on Rh nanoparticles, as predicted by DFT, are caused by a combination of lateral adlayer relaxation and the expansion of M−M bonds that also increase the distance between adsorbates, as observed in prior work.[47] M−M bonds expand as Rh atoms bond to CO*, transferring electrons from the metal to the adsorbate, thus weakening M−M bonds. M−M bond lengths between surface atoms—where this expansion is most pronounced—increase up to 3% at higher coverages on the CO*-saturated Rh_{201} particle (Figure 7a,b). We also optimized Rh_{201} particles covered in CO* with all Rh atoms frozen to remove the effects of M−M expansion on CO* binding energies, thus mimicking Rh(111), whose surface cannot expand because of the constrained periodicity of single-crystal calculations. Here, the average differential binding energy of CO* becomes less negative by 5−20 kJ mol^{-1} relative to the fully relaxed particle (Figure 7c). For example, $\Delta\bar{E}_{diff}$ values increase from −171, −154, and −118 kJ mol^{-1} to form the 1.0 ML c,e,t adlayer on a relaxed Rh_{201} particle to −164, −144, and −108 kJ mol^{-1} with the particle frozen—an average increase of 9 kJ mol^{-1}—with similar increases to form the 1.10 ML be_{10},be_{11},t adlayer (Figure 7c). While these frozen particles have less exothermic $\Delta\bar{E}_{diff}$ values, binding on frozen particles is still significantly more exothermic than on Rh(111) surfaces at similar coverages, where the ΔE_{diff} to reach 1 ML is +44 kJ mol^{-1}.

We further examine the role of M−M expansion during adsorption by calculating CO* binding energies to Rh(111) surfaces stretched by 2−10%, which introduces strain in the surface and alters the catalytic behavior of Pt-group catalysts.[104−106] As the Rh(111) surface expands, CO* binds more strongly and this stronger binding becomes more pronounced at higher coverages (Figure 8a). Surface expansion has a larger effect on atop-bound CO* than on CO* bound to threefold sites, making binding energies more negative at 1.0 ML for atop modes by 129 kJ mol^{-1} but only 89 kJ mol^{-1} for threefold—the preferred configuration without expansion (Figure 8b). These calculations partly illustrate why atop modes are more strongly preferred on particles than on Rh(111) surfaces: M−M expansion reduces coadsorbate repulsion more for atop-bound CO* than threefold CO*. These calculations on expanded surfaces show that, even at 10% expansion, binding energies do not reach those observed on the Rh_{201} particles at identical coverages (1.00 ML), while the expansion that occurs on Rh_{201} particles is just over 2% at 1.00 ML on Rh_{201}. These data show that the predominant decrease in differential binding energies as a function of coverage on particles compared to flat periodic surfaces is not caused by M−M expansion but instead by the ability of the adlayer to laterally relax because of the curvature of the surface, which allows CO* to "fan out" and maximize distances

https://doi.org/10.1021/acs.jpcc.1c05160
J. Phys. Chem. C XXXX, XXX, XXX−XXX

between adjacent C and O atoms such that adsorbates are further spaced than the M−M bonds.

We determine the degree of curvature in the adlayer by calculating the average distance between vicinal Rh atoms (described above) as well as between C and O atoms in neighboring CO*. These average C−C (x_C) and O−O (x_O) distances represent the diameters of available space surrounding these atoms for their respective positions in the adlayer. The C atoms, because they are closer to the surface, form an approximate sphere of a smaller radius than the O atoms; as such, the average distance between neighboring C atoms is always smaller on these curved particle models, and the difference between these two distances reflects the degree of curvature of the underlying surface that extends through the adlayer. The c,e,0.6×t_{111} (0.75 ML), c,e,0.6×t_{111},t_{100} (0.80 ML), and c,e,t (1.00 ML) adlayers on the Rh_{201} particle are compared to the Rh(111) surface with 1.0 ML of atop-bound CO* from Figure 8b. The average binding energy (ΔE_{avg}) to form a given CO* adlayer on the Rh(111) surface becomes stronger (*i.e.*, more negative) as the surface is stretched, but these surfaces have no curvature and thus a $x_O - x_C$ difference of zero. For the Rh_{201} nanoparticle, the curved surfaces lead to $x_O - x_C$ differences near 0.4 and thus significantly stronger ΔE_{avg} (Figure 9). The $x_O - x_C$ differences decrease with

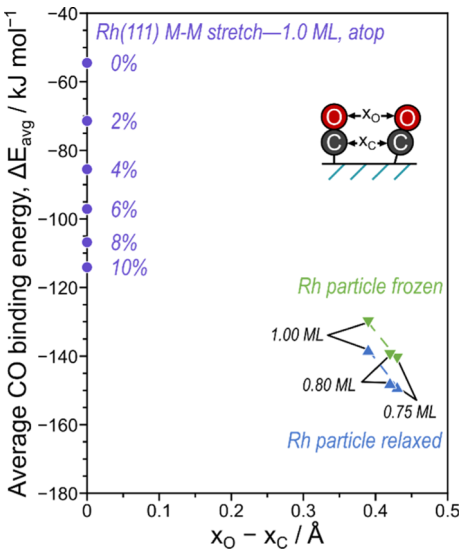

Figure 9. Average CO* binding energy (ΔE_{avg}) as a function of the difference between the average O−O distances (x_O) and average C−C distances (x_C) of neighboring CO* on differently sized Rh(111) surfaces at 1.0 ML with all CO* bound atop (●, purple) and the Rh_{201} particle with the metal atoms allowed to relax (▲, blue) and frozen (▼, green) for the three highest coverages tested with all CO* bound atop: c,e,0.6×t_{111} (0.75 ML), c,e,0.6×t_{111},t_{100} (0.80 ML), and c,e,t (1.00 ML).

increasing coverage, as shown by the data at 0.75 and 0.80 ML on Rh_{201}, and this leads, in part, to the lower ΔE_{avg} at higher coverages. Figure 9 shows that M−M stretching alone cannot account for the significantly lower ΔE_{avg} values on particles than on surfaces by comparing stretched Rh(111) surfaces and Rh_{201} particles in which the metal cluster is frozen (and thus cannot expand). Instead, we suggest that the curvature is the dominant factor in controlling ΔE_{avg} at high coverages. While curvature decreases with particle size, large particles may restructure to roughen their surfaces so as to increase their curvature and reduce the size of flat regions, as shown in prior work studying CO* on Pt nanoparticles[83,84] and other metal surfaces.[107−111]

Next, we examine how frequencies are affected by coverage, dipole−dipole coupling, and metal expansion. Surface expansion also decreases the maximum calculated frequency for CO* for all CO* coverages (Figure 8c). When the surface expands, the distance between coadsorbates increases; simultaneously, M−M bonds weaken, which should also cause M−C bonds to become stronger and possibly further decrease C−O stretching frequency. Notably, frequencies decrease by 16−25 cm^{-1} between the original Rh(111) and the surface expanded by 10% at all coverages from 0.11 to 1.0 ML and do not vary systematically with coverage for a given surface expansion. This indicates that such surface expansion alters the electronic properties of adsorbates to decrease frequencies more so than reducing adlayer strain. Such changes are akin to the catalytic changes induced by surface strain, which alters the electronic properties of metal catalysts,[104,106] in this case reflected in the stronger binding of CO* and its decreased stretching frequency with surface expansion.

Next, we turn to frequencies calculated for CO* on Rh nanoparticles to provide direct comparisons between these saturated adlayers and those examined by FTIR studies (Section 3.2). First, we calculate the individual frequencies of CO* in unique binding configurations at low coverages and within saturated adlayers (at 1.00 and 1.10 ML CO*) to examine how coordination and coverage affect individual adsorbates. For single CO* on the otherwise bare particle, vibrational frequencies vary from 1965 to 1996 cm^{-1} for atop-bound CO*, with larger frequencies when bound to metal atoms with a higher CN (Figure 10), correlating with the binding energy (Figure S7, Supporting Information). These values are in agreement with the observed vibrational frequencies of ∼1989 cm^{-1} for the atop CO* species in the experimental system at 723 K. For CO* bridge-bound to edges, the frequencies are 1814 and 1821 cm^{-1} on the be_{11} and be_{10} sites, again closely matching observed frequencies for bridge-bound CO* on small Rh clusters (1810−1838 cm^{-1} for $Rh_n(CO)$, n = 7−12).[79] However, no high-temperature bridge or threefold features are seen in the FTIR data, suggesting that the surface may prefer the atop sites at low coverages and high temperatures on the 10 wt % sample studied in this work. CO* vibrational frequencies increase as coverage increases on Rh_{201} particles. At saturation coverages, the vibration of a single CO* in frozen adlayers in these same sites range from 2001 to 2019 cm^{-1} for atop-bound CO*, an average frequency increase of 30 cm^{-1}, and for bridge-bound CO*, the frequencies both increased to 1908 cm^{-1}, an average increase of 91 cm^{-1} (Figure 10). However, these results lack the dipole−dipole coupling associated with the coordinated vibrations that can only be estimated when the frequencies of multiple CO* within the adlayer are calculated. Therefore, we turn to frequencies with more of the adlayer permitted to vibrate to compare these models to experimental results.

We also computed frequencies with varying fractions of the adlayer permitted to vibrate centered around a (111) terrace for the two possible CO*-saturated particles at three coverages. CO* frequencies increase from 2012 cm^{-1} for a single vibrating CO* on the (111) terrace on the 1.00 ML (c,e,t) adlayer to 2067 cm^{-1} with 70 vibrating CO* arranged centrally around a single (111) terrace, which represents the 57% of the adlayer, and to 2078 cm^{-1} when all CO* are in motion (Figure

https://doi.org/10.1021/acs.jpcc.1c05160
J. Phys. Chem. C XXXX, XXX, XXX−XXX

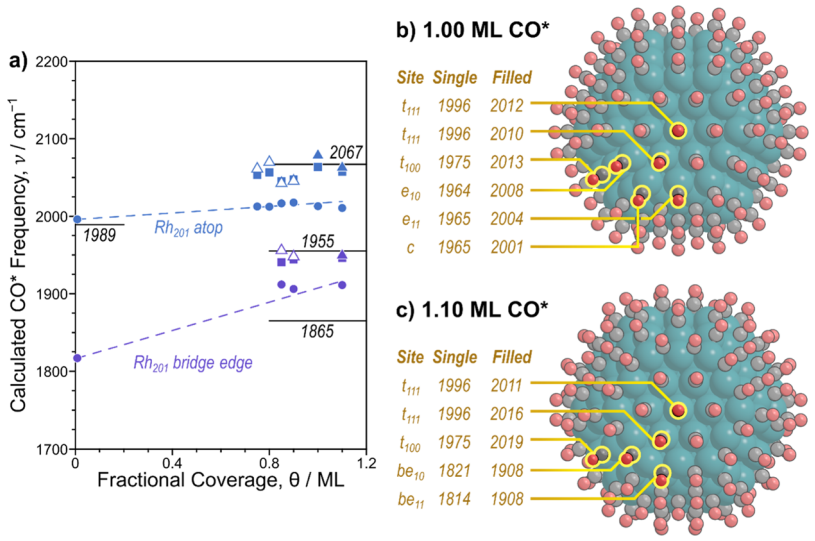

Figure 10. (a) Individual stretching frequencies (●) and the maximum calculated frequency with ∼42% of CO* permitted to vibrate (■; see Figure 11), and for 100% of CO* permitted to vibrate (▲) calculated for the 1.00 and 1.10 ML configurations (filled) and linearly extrapolated to full vibration for lower coverages (empty) for each adlayer configuration in cm^{-1} as a function of coverage Rh_{201} nanoparticles for atop binding modes (blue) and bridge-edge binding modes (purple). Frequencies of (b) atop-only (c,e,t) and (c) mixed bridge-edge and atop (be_{10},be_{11},t) CO* on the Rh_{201} particle at their saturation coverages. Frequencies are shown for an isolated CO* in the labeled binding location absent other adsorbates and on the saturated particle. Dashed lines in (a) are to guide the eye.

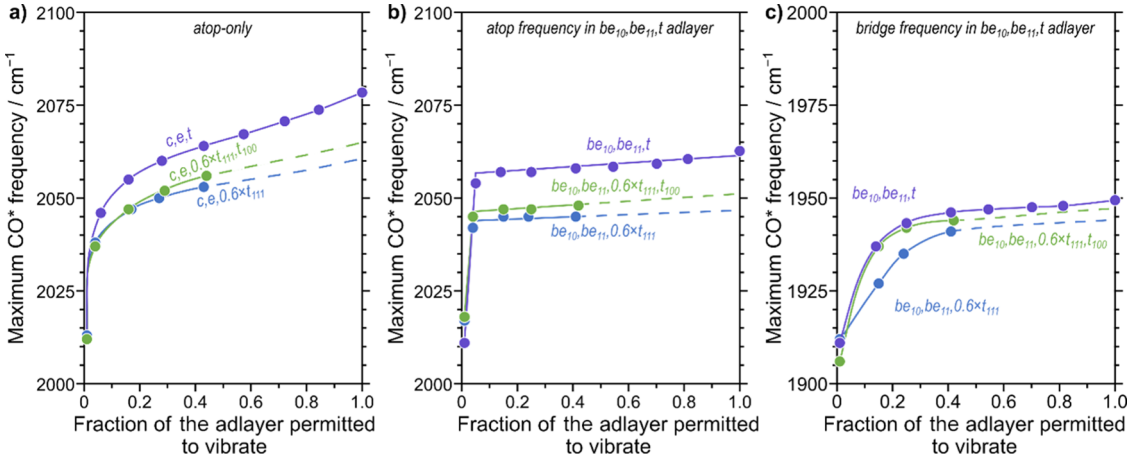

Figure 11. Highest frequencies calculated as the number of CO* permitted to vibrate on Rh_{201} increases for (a) atop-only adlayer configurations, (b) atop mode for the adlayer configurations with bridge-edge and atop modes, and (c) bridge mode for the adlayer configurations with bridge-edge and atop modes with all terrace atoms occupied (purple), the (100) terraces and part of the (111) terraces occupied, and with only part of the (111) terraces occupied. Lines are guides to the eye.

11). These high frequencies are remarkably consistent with the frequency observed experimentally at low-temperature (high-coverage frequency of 2067 cm^{-1}; Figure 5). Similar increases are observed for atop-only modes with part of the (111) terraces filled (the c,e,0.6×t_{111} and c,e,0.6×t_{111},t_{100} adlayers, with coverages of 0.75 and 0.80 ML, respectively), albeit with lower frequencies because coverages remain lower. These data indicate that for these atop-only CO* adlayers, frequencies increase nonlinearly because the dipole−dipole coupling is disrupted (but not eliminated) by the curvature of the adlayer and incomplete alignment of the CO*.

Similar increases occur for CO* on the be_{10},be_{11},t adlayer, which has a slightly higher saturation coverage (1.10 ML), but not all CO* occupy atop modes. In this case, the frequency increases from 2011 cm^{-1} for a single CO* vibration to 2054 cm^{-1} when the seven CO* in the same (111) terrace are allowed to vibrate (∼6% of the adlayer). However, the frequencies do not continue to increase significantly above this point, increasing only to 2057 cm^{-1} with 55 vibrating CO* (41% of the adlayer) and to 2063 cm^{-1} with all CO* vibrating (Figure 11b). Notably, the highest calculated frequency when 100% of the adlayer is in motion (2063 cm^{-1}) is closer to the experimentally observed value (2067 cm^{-1}) than for the full vibrating c,e,t adlayer (2078 cm^{-1}). This further indicates that adlayers are comprised of mixed binding modes. The same behavior is observed when the terraces are partly filled in the be_{10},be_{11},0.6×t_{111},t_{100} and be_{10},be_{11},0.6×t_{111} configurations, although with lower frequencies of 2048 and 2045 cm^{-1} with 42 and 41% of the adlayers vibrating, respectively. These data indicate that dipole−dipole coupling of vibrational modes is disrupted by the bridge-bound CO* that occupy the corners and edges of the particles in this adlayer arrangement. Notably,

https://doi.org/10.1021/acs.jpcc.1c05160
J. Phys. Chem. C XXXX, XXX, XXX−XXX

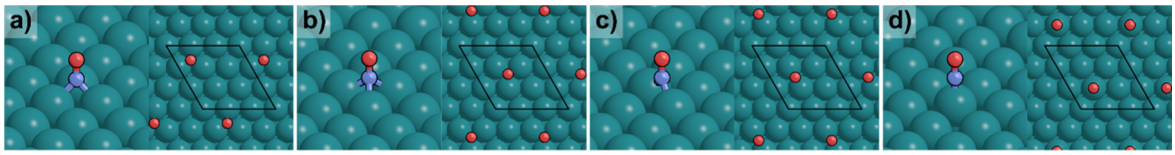

	3-fold hcp				3-fold fcc				bridge				atop			
	Binding E_0		ν_{NO}		Binding E_0		ν_{NO}		Binding E_0		ν_{NO}		Binding E_0		ν_{NO}	
RPBE	**−211**	*(0)*	**1532**	*1503*	**−210**	*(1)*	**1531**	*1503*	**−196**	*(15)*	**1636**	*1605*	**−174**	*(38)*	**1862**	*1827*
PBE	**−241**	*(0)*	**1539**	*1523*	**−239**	*(2)*	**1542**	*1527*	**−222**	*(19)*	**1645**	*1629*	**−194**	*(47)*	**1874**	*1856*
BEEF	**−217**	*(0)*	**1528**	*1513*	**−216**	*(1)*	**1531**	*1516*	**−201**	*(16)*	**1627**	*1611*	**−172**	*(45)*	**1848**	*1830*
PW91	**−240**	*(0)*	**1535**	*1522*	**−239**	*(2)*	**1538**	*1525*	**−221**	*(19)*	**1632**	*1617*	**−188**	*(53)*	**1854**	*1838*
PW/US	**−237**	*(0)*	**1559**	*1528*	**−237**	*(1)*	**1567**	*1536*	**−217**	*(20)*	**1655**	*1623*	**−178**	*(59)*	**1863**	*1827*

Figure 12. Single NO* bound (a) at a threefold hcp site, (b) at a threefold fcc site, (c) in a bridge position, and (d) atop Rh(111). Binding energies (kJ mol^{-1}), relative energies (in parentheses, kJ mol^{-1}), and NO* stretching frequencies (ν_{NO}, cm^{-1}), both scaled (bold) and unadjusted (italicized), are shown for each configuration in four exchange−correlation functionals (RPBE, PBE, BEEF, and PW91) with PAW basis sets and with the PW91 functionals using USPP (PW/US).

increasing the number of vibrating CO* also leads to higher frequencies (near 1945 cm^{-1}) for CO* bound in the bridge sites along the edges of the particle, although the increase is slightly weaker than that for atop-bound CO*. This value for CO* bound in bridging modes (1949 cm^{-1} for all CO* vibrating at 1.10 ML) is also similar to the experimental value (1955 cm^{-1}). The peak observed at 1865 cm^{-1}, typically attributed to threefold-bound CO*, is within the range of values observed for bridge-bound CO* (1814 cm^{-1} at low-coverage to 1949 cm^{-1} at high coverage) but may also reflect CO* bound in threefold sites at high coverages that are present because of disorder in the CO* adlayer or because of the existence of a small number of very large Rh particles in the experimental system that contain extended (111) domains. This entropy-driven disorder is absent from the idealized models used in DFT studies but may persist even at high coverages, leading to adlayers in which the majority of CO* occupy atop sites with a small fraction of threefold-bound CO*. These calculated CO* vibrational frequencies and site preferences at different coverages on Rh_{201} match experimental data on Rh nanoparticles and deviate from previous experimental results and our calculations for CO* on Rh(111). Thus, while we could not experimentally assess saturation CO* coverage accurately on Rh nanoparticles, the trends observed during TPD strongly support the assertion that Rh nanoparticle DFT models capture the experimental system that mimics industrial catalysts better than flat surfaces.

3.5. DFT-Calculated NO Binding on Rh(111) Surfaces.

NO adsorption energies on Rh(111) surfaces and Rh_{201} particles have been reported in our recent work.[46] In brief, NO* prefers to bind in threefold hcp sites at low coverages in all functionals tested, although threefold fcc sites are only 1−2 kJ mol^{-1} less stable (Figure 12). Notably, when an isolated NO* is bound atop to Rh(111), it is linear (Figure 12d) rather than bent, and optimizations of bent configurations caused them to become linear, indicating that the bent state is not a local minimum in the potential energy surface at these coverages. As NO* coverage increases, NO* remains in threefold sites, with similar binding energies for the threefold hcp and threefold fcc binding modes and occupying a mixture of hcp and fcc binding modes from 0.33 to 0.78 ML (Figure S11, Supporting Information). Rh(111) saturates with NO* at 0.67 ML at 473 K, as differential NO binding free energies (ΔG_{diff}) remain negative up to this coverage, consistent with surface science experiments (Figure 13a).[28]

Previous surface science studies showed that the vibrational frequency of NO* at 0.1 ML was 1512 cm^{-1} and attributed this to threefold-bound NO* on Rh(111);[28] this observed frequency is similar to the frequency estimated here (1531 and 1532 cm^{-1} for NO* in threefold fcc and hcp sites, respectively, using RPBE, PAW). Similar to CO* frequencies, those for NO* also increase as NO* coverage increases (Figure 13b). Frequencies calculated with their dipole moments show that the maximum computed frequency has an estimated intensity larger than that of all other frequencies such that it should be the dominant feature in IR spectra at all coverages, as for CO* (Table S4, Supporting Information); therefore, we again focus on the maximum calculated frequency for NO* on Rh(111), as with CO*. This maximum frequency increases with coverage from 1532 cm^{-1} at 0.11 ML to 1696 cm^{-1} at 0.67 ML—the NO* saturation coverage on Rh(111)—and to 1742 cm^{-1} at 1.00 ML (Figure S12, Supporting Information). This increase is similar to the increase in observed frequencies in ultrahigh vacuum experiments of NO adsorption to Rh(111), where observed frequencies increased from 1513 cm^{-1} at 0.1 ML to 1633 cm^{-1} near 0.68 ML.[28] The gap between the measured and calculated frequencies increases with NO* coverage, such that DFT overpredicts the increase in NO* frequencies with coverage; however, the NO* adlayers in the EELS data include a mixture of NO* bound to bridge, atop, and threefold sites, albeit primarily threefold. The effects of vibrational coupling are only observed for adsorbates within the same binding modes, so the shift in threefold NO* frequencies is smaller in the EELS data for the adlayers with mixed binding modes. As with CO*, differences are expected between a Rh(111) single-crystal surface and a supported particle, and as such, we approximate the latter using Rh_{201} particles.

3.6. NO Binding to Rh_{201} Nanoparticle Models.

Adsorption energies for NO* on Rh_{201} particles have been published in our recent work.[46] NO first binds atop to corner (c) sites ($\Delta\bar{E}_{diff}$ = −239 kJ mol^{-1}), followed by bridge sites along the edges (be_{10} and be_{11}, $\Delta\bar{E}_{diff}$ = −202 kJ mol^{-1}) before adsorbing to hcp sites on (111) terraces (hcp) and to bridge sites between (100) terrace and edge atoms (bt_{10}) ($\Delta\bar{E}_{diff}$ = −101 kJ mol^{-1}), saturating at 1.38 ML (Figure 14b−f). Similar to CO*-filling calculations on Rh_{201}, we investigated additional NO* binding configurations that were less favorable than the pathway outlined above (orange dots in Figure 14a). Differential binding energies for NO* on the particles are ∼30−200 kJ mol^{-1} more exothermic for NO* adsorption onto the Rh_{201} particle than the Rh(111) single-crystal surface at

https://doi.org/10.1021/acs.jpcc.1c05160
J. Phys. Chem. C XXXX, XXX, XXX−XXX

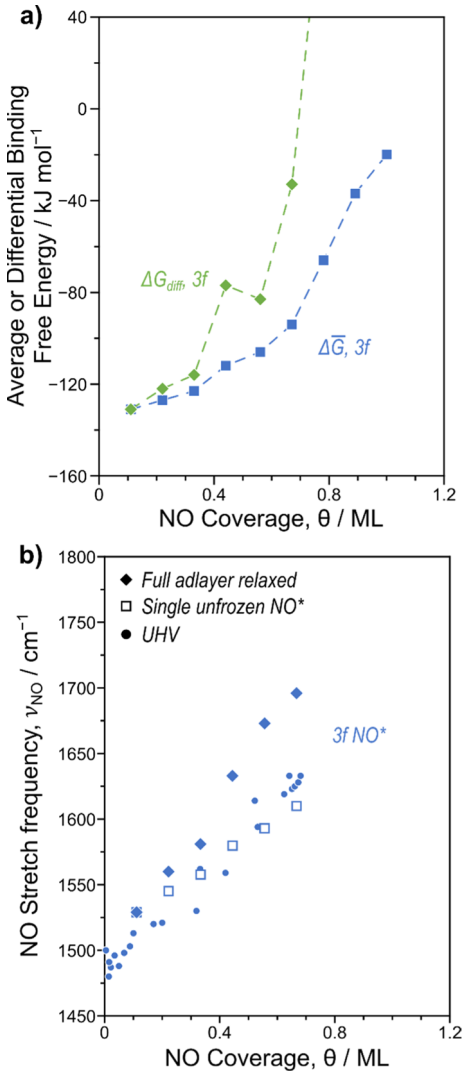

Figure 13. (a) Average binding free energies (473 K, 1 bar) of NO on Rh(111) surfaces in threefold (■, blue) binding modes (which are always preferred) and the differential binding free energy (ΔG_{diff}; 473 K, 1 bar) for the best configuration (◆, green), the full set of data up to 1.0 ML is shown in Figure S12 of Supporting Information. (b) Maximum calculated NO* stretching frequency for best configuration with the entire adlayer permitted to move (◆) and with only one NO* permitted to move (■, hollow) from 0 to 0.67 ML NO* threefold (blue) binding modes. Pale dots in (b) show experimental EELS data from Root *et al.* (95 K, 10^{-8} to 10^{-6} Torr NO).[28]

similar coverages. As described for CO*, this difference arises because of a combination of M−M bond extension (up to 7.4% increase at 1.38 ML for Rh_{201})—most significantly between surface metal atoms—and because of the ability of the adlayer to laterally expand—most prominently for NO* bound to corner and edge sites—in a manner that is impossible on a periodic single-crystal model, leading to longer N−N and O−O distances in the adlayer and reduced adsorbate−adsorbate repulsion.

Next, we evaluate the effect of expanding the Rh(111) surface on NO* binding energies and frequencies to separate the effects of the model geometry and the M−M expansion. Surface expansion reduces NO* differential binding energies by more than it does for CO* (Figure 15a). Given a 10% expansion of the metal surface, ΔE_{diff} becomes more negative (strengthens) by 36 kJ mol^{-1} for CO* and 49 kJ mol^{-1} for NO* at 0.11 ML, and they strengthen by 89 and 129 kJ mol^{-1}, respectively, at 1.00 ML. The greater effect of M−M expansion on the binding energies of NO* than CO* suggests stronger coadsorbate repulsions among NO* and is consistent with the larger M−M expansion observed for NO* adsorption on Rh_{201} (7.4%) than for CO* on Rh_{201} (3.0%) at saturation. The stronger coadsorbate repulsions between NO* may arise from its binding mode in threefold sites rather than atop sites, the latter of which yields less coadsorbate repulsion because metal-atom sharing among coadsorbates does not occur.

When examining NO* frequencies on stretched surfaces, we omit adlayers that contain bridge-bound NO* to focus on how the frequencies of threefold-bound NO* change with coverage and metal expansion. The highest calculated stretching frequencies decrease by 50−80 cm^{-1} with 10% surface expansion, with a general linear decrease with expansion that is consistent at different coverages, leading to the nearly parallel lines in Figure 15b. The effects of M−M expansion on NO* frequencies are greater than on CO* frequencies, concomitant with the larger changes in adsorption energies. At 1.0 ML, this highest NO* frequency decreases by 57 cm^{-1} from 1744 cm^{-1} with no expansion to 1687 cm^{-1} with 10% expansion, while for CO* bound only atop, the highest frequency decreases by 25 cm^{-1} from 2126 to 2101 cm^{-1}. These results indicate that frequencies on unexpanded Rh(111) surfaces at high coverages are potentially overestimated compared to those expected on Rh particles—which expand upon NO* adsorption—at similar coverages.

We also calculate frequencies for NO* in its unique binding positions on the saturated (1.38 ML adlayer) Rh_{201} particle. At low coverages (single NO*), adsorption frequencies range from 1499 to 1811 cm^{-1}, with frequencies generally increasing for NO* bound to smaller metal ensembles (*i.e.*, atop *vs* threefold). NO* bound to three distinct threefold hcp sites on the (111) terrace vibrate at frequencies from 1499 to 1513 cm^{-1} with NO* frequencies decreasing as their threefold ensembles incorporate more edge atoms which have a lower coordination number (7) than those in the (111) terrace (9). NO* bound in bridge sites vibrate at 1619 cm^{-1} (bt_{10}) and 1653 cm^{-1} (be_{11}). NO* bound linearly atop corner atoms vibrate with the highest frequencies of 1811 cm^{-1}. Similar to CO*, NO* frequencies generally increase as coverages increase on the particles and as the number of NO* vibrating in the adlayer increases. For a single NO* vibrating within the 1.38 ML adlayer, frequencies increase by ∼80 cm^{-1} for bridge- and threefold-bound NO* (Figure 16). Notably, the frequency of atop-bound NO* on the corner of the saturated particle decreases from 1811 to 1756 cm^{-1} as coverage increases from 0.01 to 1.38 ML, and the NO* shifts from a linear binding mode to a bent mode; such a change indicates that NO* might possess partial negative charge characteristic of bent atop NO*. This is also in contrast to atop-bound NO* on the Rh(111) surface, which did not adopt bent configurations at any coverage, indicating that such bent NO* configurations are primarily accessible on undercoordinated Rh. These high-coverage frequencies (near 1580, 1680, and 1800 cm^{-1}) are from a single NO* vibrating within an otherwise fixed adlayer and thus are underestimates of true values because they omit the effects of coupled vibrations.

The majority of the 1.38 ML NO* adlayer consists of NO* bound to threefold hcp sites on the (111) terraces: these comprise 96 NO* (57%) of the total 168 NO*, with another

https://doi.org/10.1021/acs.jpcc.1c05160
J. Phys. Chem. C XXXX, XXX, XXX−XXX

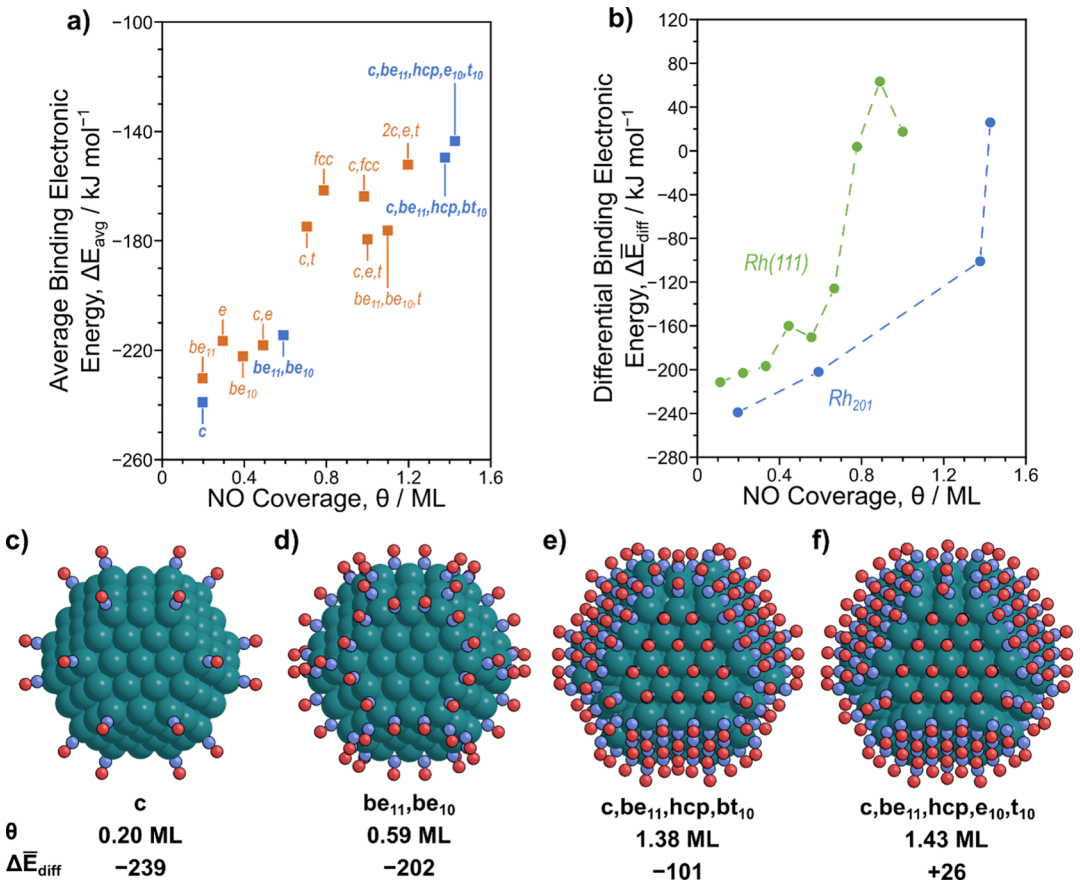

Figure 14. (a) Overall average NO binding energies on the Rh_{201} nanoparticle (■) with the most likely configurations to fill the particle (blue) and all other configurations tested that optimized without adlayer reorganization (orange). (b) Average differential (●) electronic binding energies for NO as a function of coverage on the Rh(111) surface (green) and on the Rh_{201} particle model (blue). Configuration of NO* at (d) 0.20, (e) 0.59, (f) 1.38, and (g) 1.43 ML on the Rh_{201} particle.

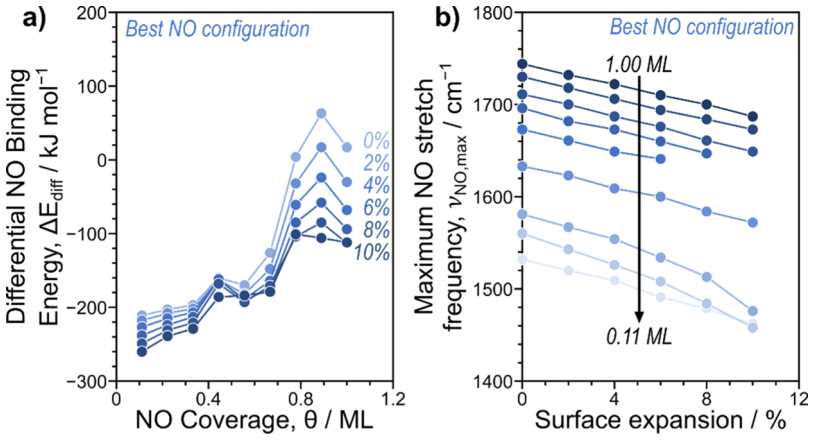

Figure 15. (a) Differential NO* binding energies (ΔE_{diff}) on the Rh(111) surface as the unit cell was expanded 0−10% in 2% increments (light to dark blue with increasing expansion) for the most stable NO* configuration and (b) highest calculated frequency for the configurations shown in (a) from 0.11 ML (light blue) to 1.0 ML (dark blue) as the unit cell expands.

24 NO* bound to corner sites, bt_{10} sites, and be_{10} sites each (14% each). The vibrational frequency of the center-most hcp NO* on an otherwise bare surface is 1513 cm^{-1}, which increases to 1595 cm^{-1} in a frozen adlayer at 1.38 ML. Here, we increase the number of NO* allowed to vibrate in these frequency calculations from 1 to 168 (the entire adlayer) centered around a single (111) terrace to estimate the vibrational frequencies at saturation on Rh particles, similar to our approach for CO* (Figure 10). The highest frequency increases from 1595 cm^{-1} (1 NO* vibrating) to 1664 cm^{-1} when all 12 NO* bound in hcp sites on the (111) terrace vibrate (Figure 17). Including vibrations of NO* bridge-bound on (100) terraces (bt_{10}) does not affect the threefold hcp maximum frequency because these NO* vibrational modes do not couple despite having similar frequencies (both near 1670 cm^{-1}). Similar effects are observed for the inclusion of NO*

https://doi.org/10.1021/acs.jpcc.1c05160
J. Phys. Chem. C XXXX, XXX, XXX−XXX

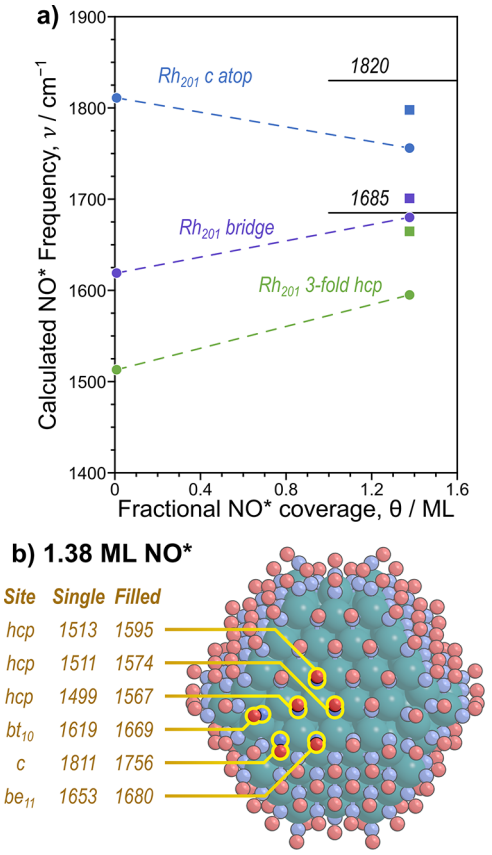

Figure 16. (a) Individual stretching frequencies (●) and the maximum calculated frequency with the largest number of NO* permitted to vibrate calculated in this work for each adlayer configuration (■; see Figure 17) in cm^{-1} as a function of coverage Rh_{201} nanoparticles for atop binding modes on c sites (blue), bridge binding modes on be_{11} and bt_{10} sites (purple), and hcp binding modes at different locations on the (111) terrace (green). (b) Frequencies of individual NO* on the saturated Rh_{201} particle (c,be_{11},hcp,bt_{10}). Frequencies are shown for an isolated NO* in the labeled binding location absent other adsorbates and on the saturated particle. Dashed lines in (a) are to guide the eye.

binding to be_{11} sites or to corner sites, with negligible effects on the frequency of hcp-bound NO*, indicating that little dipole−dipole coupling is observed between NO* bound on distinct binding modes, even if these modes have similar frequencies. The inclusion of additional NO* in threefold modes on other terraces also does not influence the maximum frequencies, which reach 1665 cm^{-1} when the entire adlayer vibrates because NO* do not vibrationally couple between distinct terraces. This behavior differs from CO* in the 1.00 ML adlayer in which all CO* are bound in atop sites (Figure 10), where some dipole−dipole coupling does occur between distinct facets despite the changes in CO* orientation. Similar behavior occurs for bridge-bound NO* on the edges between (111) terraces on the particle: permitting more NO* to vibrate does not significantly change their frequencies as the fraction of the adlayer allowed to vibrate increases from 16% (1698 cm^{-1}) to 100% (1701 cm^{-1}; Figure 17). In contrast, frequencies for atop-bound NO* on corner sites and bridge-bound NO* on bt_{10} sites do continue to increase as more of the adlayer vibrates in these calculations, reaching 1798 cm^{-1} for corner-bound NO* and 1684 cm^{-1} for bt_{10} NO* with 100% of the adlayer in motion.

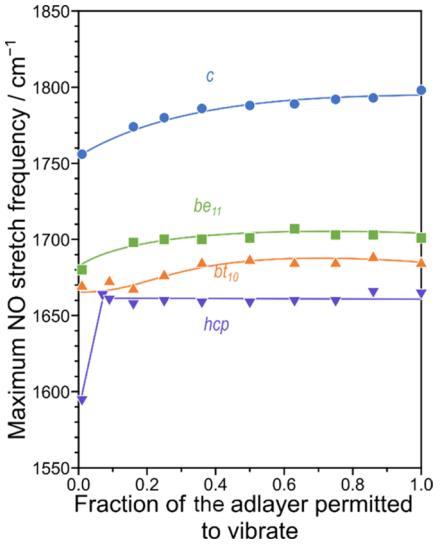

Figure 17. Highest calculated frequencies as the number of NO* permitted to vibrate on Rh_{201} increases in the c,be_{11},hcp,bt_{10} adlayer configuration (1.38 ML NO*) for NO* bound in hcp (●, blue), bt_{10} (■, green), be_{11} (▲, orange), and atop (▼, purple) binding modes. Lines are guides to the eye.

3.7. NO and NO−CO Probe Molecule FTIR Spectroscopy. The NO* and CO* adsorption energies on both the Rh(111) and Rh_{201} catalyst models suggest that NO* should dominate surfaces of Rh catalysts at CO/NO ratios of 3−30 that are typical of automotive exhaust conditions. Here, this is probed experimentally by comparing FTIR spectra for CO−NO mixtures at reaction conditions (5000 ppm CO, 1000 ppm NO, 478 K) to the catalyst saturated in CO or NO at room temperature (298 K) on 10 wt % Rh/γ-Al_2O_3 (Figure 18). Both the CO−NO mixture and NO-saturated spectra contain a peak at 1685 cm^{-1}, with a prominent shoulder at 1640 cm^{-1} and a smaller peak at 1820 cm^{-1}. These features have been

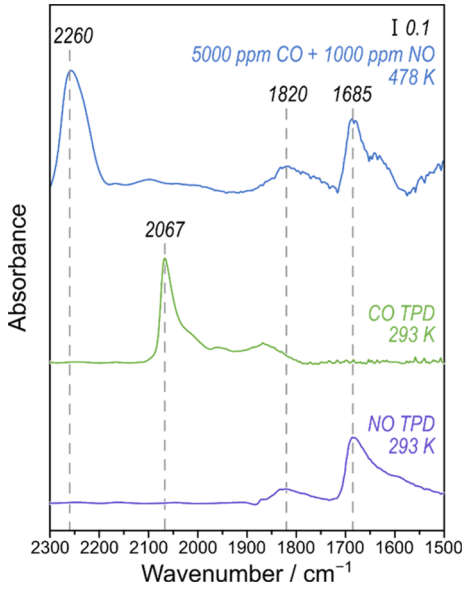

Figure 18. IR spectra of 10 wt % Rh/γ-Al_2O_3 in 5000 ppm of CO/1000 ppm NO at 478 K (blue), at 293 K after saturation with CO before TPD (green; also in Figure 5), and at 293 K after saturation with NO before TPD (purple; also in Figure 20).

https://doi.org/10.1021/acs.jpcc.1c05160
J. Phys. Chem. C XXXX, XXX, XXX−XXX

observed previously for NO* on supported Rh catalysts (1.0 wt % Rh/Al_2O_3, 6 kPa NO, 300 K)[112] but are inconsistent with the 1512 cm^{-1} observed at low coverage and the dominant peak near 1630 cm^{-1} at saturation coverage on Rh(111) single-crystal surfaces (0.67 ML).[28] Conversely, the peak at 2067 cm^{-1} observed in the spectra associated with CO* saturated Rh particles, corresponding to atop-bound CO*, does not appear in the spectrum for the CO−NO mixture. The similarities between the NO-saturated and CO−NO mixture spectra suggest that NO* dominates the surfaces of Rh catalysts at a 5:1 ratio, consistent with DFT predictions. Furthermore, the spectral features at 1640 and 1685 cm^{-1} are very similar to calculated vibrational frequencies of NO* at high coverage for NO* bound to threefold and bridging sites, which range from 1660 to 1700 cm^{-1} (Figure 17). The feature at 1820 cm^{-1} is in qualitative agreement with the prediction for NO* bound atop corner atoms on Rh_{201} particles (1780 cm^{-1}). An additional peak at 2260 cm^{-1} is only present in the spectrum of the CO−NO mixture at reaction conditions (478 K); thus, it is likely associated with a byproduct of CO−NO reactions, among which NCO* species are likely as NCO* has been reported to spillover onto γ-Al_2O_3 supports and have frequencies near 2260 cm^{-1}.[4]

These spectra suggest that NO* dominates Rh surfaces in mixed NO−CO feeds. DFT exchange energies of CO* with NO* directly on CO* or NO* covered surfaces are consistent with this observation. The first CO* and NO* bind with ΔG_{diff} of −53 and −105 kJ mol^{-1}, respectively, at 473 K and 1 bar; this can be shown as an NO−CO exchange energy of +52 kJ mol^{-1} (Figure 19). These exchange energies are >30 kJ mol^{-1}

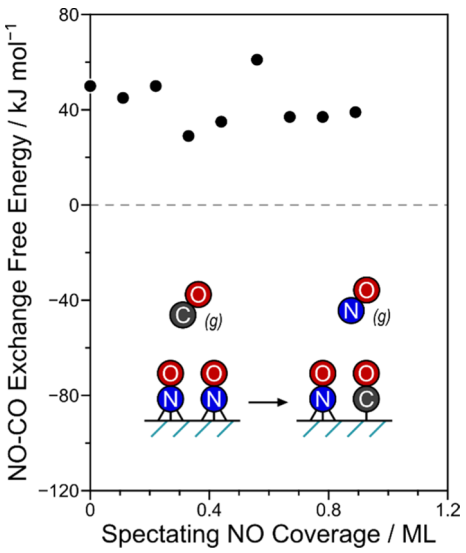

Figure 19. Free energy to exchange NO for CO at a range of spectating NO coverages on Rh(111) (473 K, 1 bar).

at all NO* coverages on Rh(111), indicating that NO* always outcompetes CO* for adsorption sites at equal pressures (Figure 19). The exchange probability can be computed as

$$\frac{K_{CO}P_{CO}}{K_{NO}P_{NO}} = \exp\left(-\frac{\Delta\Delta G_{NO-CO}}{k_b T}\right)\left(\frac{P_{CO}}{P_{NO}}\right) \quad (8)$$

where $\Delta\Delta G_{NO-CO}$ is the coverage-dependent NO−CO exchange free energy. Given the large positive values of this exchange energy, very large CO/NO ratios (>10^4) would be required for a favorable displacement of NO* by CO* on Rh(111) if exchange is quasi-equilibrated, and these ratios are much greater than NO−CO reduction conditions (≤10^2). Similarly, we compute NO−CO exchange electronic energies ($\Delta\Delta E_{NO-CO}$) on Rh_{201} particles by replacing one adsorbate on the NO*-saturated Rh_{201} with CO*. These $\Delta\Delta E_{NO-CO}$ range from +21 kJ mol^{-1} on corner sites to +55 kJ mol^{-1} on hcp sites (Figure S17, Supporting Information). Conversely, replacing CO* with NO* on CO*-covered surfaces (1.0 ML) have $\Delta\Delta E_{NO-CO}$ ranging from −24 kJ mol^{-1} (on terrace sites) to −78 kJ mol^{-1} on corners (Figure S18, Supporting Information).

3.8. NO Probe Molecule FTIR-TPD Behavior. NO*-saturated 10 wt % Rh/γ-Al_2O_3 spectral signatures were collected in flowing Ar while temperature increased by 0.33 K s^{-1} from 293 to 613 K (Figure 20a). As temperature increases, the ∼1820 cm^{-1} peak disappears and a ∼1790 cm^{-1} peak appears near 473 K before also disappearing by 593 K. The main feature (∼1685 cm^{-1}, assigned to NO* on threefold and bridging sites) shows no significant shift in peak intensity or position up to 473 K, followed by a decrease in intensity and a small shift of the peak to near 1650 cm^{-1} as the peak disappears by 573 K. This rapid change in the NO* peak behavior (over a range of 473−573 K) is in stark contrast to the gradual changes observed in CO* peak positions and intensities over the range of 293−723 K. This suggests that while the CO* adlayer is continuously undergoing desorption and rearrangement from 293 to 723 K, the NO* adlayer is essentially static from 273 to 473 K and rapidly rearranges and disappears by 573 K. Further, the NO* peak begins to disappear at 473 K, while the main CO* peak (2067 cm^{-1}) begins to disappear near 650 K; this would typically suggest that NO* binds more weakly to Rh than CO*, in direct contrast with DFT-predicted binding energies that are consistently 50 kJ mol^{-1} more exothermic for NO* than for CO* across all DFT methods examined in this work. This inconsistency suggests that the NO* peak disappearance at 473 K is not related to desorption. TPD of NO*-saturated Rh combined with mass spectrometry showed that N_2 evolves above 473 K,[25,113−117] suggesting that this low-temperature peak disappearance indicates the activation of NO* rather than its molecular desorption. This is also supported by the coincidence between change in the peak area with increasing temperature and the NO conversion light-off observed from CO−NO reactions on 10 wt % Rh/γ-Al_2O_3 catalysts from our prior work (Figure 20c).

These spectroscopic, reaction, and theoretical data suggest that Rh particles are dominated by NO* under NO−CO reaction conditions and that these NO* adlayers are less responsive to temperature changes than CO* until 473 K when they react to form vacant sites (without NO* desorption) and gas-phase products, leading to rapid light-off. This could, for example, occur *via* reaction of two vicinal NO* to form O*, N_2O gas, and a surface vacancy. Once vacancies are formed, NO* may then dissociate into N* and O*. While many reaction pathways are possible once surface vacancies are formed, the data presented here suggest that initial formation of surface vacancies must occur *via* reactions of coadsorbed NO* rather than by the desorption of NO*. The mechanism of this reaction will be examined in future work, using Rh particle DFT models, which were shown here to more accurately capture the behavior of Rh nanoparticle experimental systems compared to periodic models.

https://doi.org/10.1021/acs.jpcc.1c05160
J. Phys. Chem. C XXXX, XXX, XXX−XXX

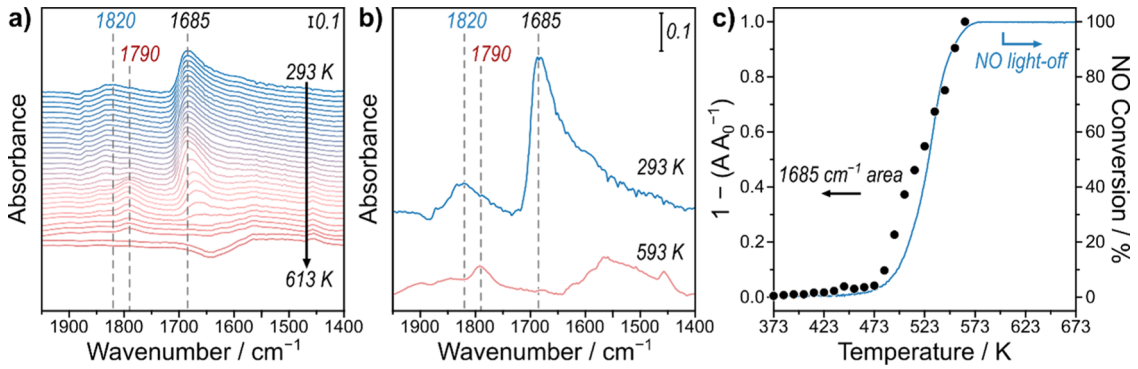

Figure 20. IR spectra of 10 wt % Rh/γ-Al_2O_3 (a) taken every 10 K as the temperature increases 0.33 K s^{-1} from 293 to 613 K after the sample is fully saturated with NO and (b) shown in detail at 293 and 593 K, identifying atop NO* (1820−1790 cm^{-1}) and threefold NO* (1685 cm^{-1}). (c) Fraction of deconvoluted 1685 cm^{-1} IR peak area loss normalized to the largest respective peak area ($1 - A{\cdot}A_0^{-1}$) on 10% Rh/γ-Al_2O_3 (●) and NO conversion (blue line) over 2 mg of diluted 10 wt % Rh/γ-Al_2O_3 catalyst (0.2 mg Rh) as a function of temperature at a ramp rate of 0.33 K s^{-1} in 5000 ppm of CO/1000 ppm NO.[2]

4. CONCLUSIONS

DFT predicts that CO* occupies a mixture of atop and threefold binding modes on Rh(111), saturating at 0.56 ML at 473 K, with vibrational frequencies for both atop and threefold CO* increasing by 45 and 91 cm^{-1}, respectively, with increasing coverage from 0.11 to 0.56 ML. DFT predicts that NO*, on the other hand, occupies only threefold binding modes at all coverages on Rh(111) surfaces, saturating near 0.67 ML, and its vibrational frequencies also increase with coverage (by ∼170 cm^{-1}) from 0.11 to 0.67 ML. These site preferences, maximum coverages, and vibrational frequencies agree well with previous experimental data on Rh single crystals. However, FTIR spectra indicate that CO* and NO* can bind in multiple configurations on a 10 wt % Rh/γ-Al_2O_3 sample consisting of only Rh nanoparticles (*i.e.,* without any atomically dispersed Rh species) with an average diameter of 2.6 nm. In CO environments, FTIR spectra have a large peak at 2067 cm^{-1}, indicating mostly atop-bound CO*, with smaller peaks at 1955 and 1850 cm^{-1} at 293 K, consistent with bridge and threefold-bound CO*. TPD studies of this adlayer show that the atop-bound CO* frequencies shift by 78 cm^{-1} as CO* desorb from the surface, which is much more than the shift of ∼55 cm^{-1} observed from 0 to 0.78 ML in HREELS data on Rh(111) and the shift of 70 cm^{-1} from DFT data on Rh(111) for the same coverages.[22] FTIR spectra of the 10 wt % Rh/γ-Al_2O_3 sample in NO have a predominant peak at 1685 cm^{-1} and a smaller peak at 1820 cm^{-1}, corresponding to threefold and atop-bound NO*. In TPD studies of the NO* adlayer, spectra are unchanged until 473 K and then rapidly disappear (by 573 K) by activation and formation of N_2 and N_2O rather than by NO* desorption. The FTIR data on a sample containing exclusively Rh nanoparticles show numerous differences from prior single-crystal and DFT studies on Rh(111) surfaces.

Our previous work showed that supramonolayer coverages are possible on metal nanoparticle models because interactions between adsorbates across periodic boundaries are absent, particle curvature permits the adlayer to laterally relax and reduce strain, and surface M−M bonds can expand on nanoparticle models.[44,46−49,69] Here, we show the same is true for CO* and NO* on 201-atom Rh nanoparticles and that the curvature of the particle is the predominant cause of the more exothermic binding energies of these adsorbates, which leads to higher coverages than those achievable on flat Rh(111) surfaces. CO* prefers to bind in atop modes on Rh_{201} particles, with some CO* binding in bridge binding modes and saturating near 1 ML, while NO* occupies a mixture of threefold, bridge, and atop sites on Rh_{201} with a saturation coverage of 1.38 ML.

Calculated CO* and NO* frequencies at various coverages and with varying numbers of adlayers permitted to vibrate during frequency calculations are used to compare these CO* and NO* adlayers to FTIR spectra. As more adsorbates are included in these frequency calculations, frequencies increase because of dipole−dipole-coupled in-phase vibrations of adsorbates in the same binding modes and because of repulsion between coadsorbates in crowded adlayers. The maximum vibrational frequency for the atop-only CO* on Rh_{201} increases from 1996 cm^{-1} at 0.01 ML to 2078 cm^{-1} with 100% of the adlayer simultaneously vibrating at 1.00 ML. These frequencies and their shift from 1996 to 2078 cm^{-1} with increasing coverage are remarkably close to those observed in the FTIR spectra for the 10 wt % Rh/γ-Al_2O_3 sample (shift from 1989 to 2067 cm^{-1}). These data illustrate how these nanoparticle models more accurately capture the preference for atop CO* binding on supported Rh particles in contrast to flat surfaces where more threefold binding occurs.

At high coverages, calculated NO* frequencies on Rh_{201} surfaces are near 1660 cm^{-1} for threefold-bound NO*, 1670 and 1700 cm^{-1} for bridge-bound NO*, and 1780 for NO* atop corner atoms. These frequencies are in good agreement with the broad band near 1685 cm^{-1} in NO* adlayer FTIR spectra at 293 K for the 10 wt % Rh/γ-Al_2O_3 sample, as well as a sharp peak at 1820 cm^{-1}. DFT underpredicts the atop-bound NO* frequency by ∼30 cm^{-1} when the full adlayer was permitted to vibrate; however, the band at 1820 cm^{-1} disappears during TPD near 473 K, with the concomitant appearance of a peak at 1790 cm^{-1}, which matches more closely with DFT-calculated frequencies. Such changes may indicate that atop-bound NO* frequencies are sensitive to particle size, adlayer arrangement, and any reaction-derived coadsorbates on the surface and that DFT estimates of these frequencies may not fully capture their behavior.

Varying the number of adsorbates in these particle adlayer calculations shows that in-phase vibrations continue to increase frequencies even between facets with distinct orientations (*i.e.,* even as the adlayer curves across the nanoparticle) but only when adsorbates are in identical modes in uninterrupted

https://doi.org/10.1021/acs.jpcc.1c05160
J. Phys. Chem. C XXXX, XXX, XXX−XXX

adlayers. The atop-only CO* adlayer (1.00 ML), for example, has maximum frequencies that linearly increase from 2055 cm^{-1} (19 vicinal CO* vibrating, 16% of the adlayer) to 2078 cm^{-1} (122 CO*, 100% of the adlayer), showing that in-phase vibrations can extend across multiple facets. However, when these atop CO* regions are interrupted by bridge-bound CO*, there is no coupling between CO* on different (111) facets, as shown by vibrational frequencies that remain nearly constant, changing from 2054 to 2063 cm^{-1} as the number of CO* vibrating changes from 19 to 134 CO* (14−100% of the adlayer) by including CO* on adjacent terraces. Similarly, NO* frequencies bound in threefold hcp sites remain constant at ∼1658 cm^{-1} as the number of NO* vibrating was changed from 12 to 168 NO* (7−100% of the 1.38 ML adlayer).

FTIR spectra at reaction conditions (5000 ppm CO, 1000 ppm NO, 478 K) resemble those in pure NO environments, indicating that NO* dominates the surfaces of the 10 wt % Rh/γ-Al_2O_3 sample under conditions similar to those of automotive exhaust, with an additional peak at 2260 cm^{-1}, showing that byproducts form (*e.g.,* NCO*). These data are consistent with the more exothermic adsorption energies for NO* compared to CO* for both Rh(111) and Rh_{201} catalyst models and for NO*−CO* exchange energies, showing that replacing NO* with CO* is endothermic on all catalyst models and at all NO* coverages.

This combined computational and experimental approach rigorously characterizes supported Rh nanoparticle catalysts and illustrates how particle curvature and metal expansion can alter binding behavior of these adsorbates. Such considerations are necessary because the binding modes and saturation coverages on metal catalysts can in turn alter their kinetic behavior. Achieving an accurate understanding of the underlying causes of these different adlayer configurations must precede computational studies of these supported catalysts.

■ ASSOCIATED CONTENT

Supporting Information

The Supporting Information is available free of charge at https://pubs.acs.org/doi/10.1021/acs.jpcc.1c05160.

> Statistical mechanics formulas used to calculate free energies and enthalpies, images of structures for CO* on Rh(111) at all tested coverages, diameter estimation for Rh particles from HRSTEM, images of structures for CO* on Rh_{201} nanoparticles, images of structures for NO* on Rh(111) at all tested coverages, images of structures for NO* on Rh_{201} nanoparticles, and images of structures where one CO* or NO* has been exchanged for the other (PDF)

■ AUTHOR INFORMATION

Corresponding Authors

Phillip Christopher − *Department of Chemical Engineering, University of California Santa Barbara, Santa Barbara, California 93106, United States;* orcid.org/0000-0002-4898-5510; Email: pchristopher@ucsb.edu

David Hibbitts − *Department of Chemical Engineering, University of Florida, Gainesville, Florida 32611, United States;* orcid.org/0000-0001-8606-7000; Email: hibbitts@che.ufl.edu

Authors

Alexander J. Hoffman − *Department of Chemical Engineering, University of Florida, Gainesville, Florida 32611, United States;* orcid.org/0000-0002-1337-9297

Chithra Asokan − *Department of Chemical Engineering, University of California Santa Barbara, Santa Barbara, California 93106, United States*

Nicholas Gadinas − *Department of Chemical Engineering, University of California Santa Barbara, Santa Barbara, California 93106, United States*

Pavlo Kravchenko − *Department of Chemical Engineering, University of Florida, Gainesville, Florida 32611, United States*

Andrew "Bean" Getsoian − *Research and Advanced Engineering, Ford Motor Company, Dearborn, Michigan 48121, United States;* orcid.org/0000-0003-1534-3818

Complete contact information is available at: https://pubs.acs.org/10.1021/acs.jpcc.1c05160

Notes

The authors declare no competing financial interest.

■ ACKNOWLEDGMENTS

This work was supported by the National Science Foundation under grant nos CBET-1803165 and 1804128, which are collaborative grants. Computational resources were provided by Extreme Sciences and Engineering Discovery Environment (XSEDE), which is supported by National Science Foundation grant number ACI-1548562, through allocation CTS160041. Electron microscopy was executed at the UCSB Materials Research Lab (MRL). The MRL Shared Experimental Facilities are supported by the MRSEC Program of the NSF under Award no. DMR 1720256, a member of the NSF-Funded Materials Research Facilities Network.

■ REFERENCES

(1) Granger, P.; Parvulescu, V. I. Catalytic NO_x abatement systems for mobile sources: from three-way to lean burn after-treatment technologies. *Chem. Rev.* **2011**, *111*, 3155−3207.

(2) Asokan, C.; Yang, Y.; Dang, A.; Getsoian, A. B.; Christopher, P. Low-Temperature Ammonia Production during NO Reduction by CO Is Due to Atomically Dispersed Rhodium Active Sites. *ACS Catal.* **2020**, *10*, 5217−5222.

(3) Granger, P.; Dujardin, C.; Paul, J.-F.; Leclercq, G. An overview of kinetic and spectroscopic investigations on three-way catalysts: mechanistic aspects of the CO+NO and CO+N_2O reactions. *J. Mol. Catal. A: Chem.* **2005**, *228*, 241−253.

(4) Yoo, C.-J.; Getsoian, A.; Bhan, A. NH_3 formation pathways from NO reduction by CO in the presence of water over Rh/Al_2O_3. *Appl. Catal., B* **2021**, *286*, 119893.

(5) Khivantsev, K.; Vargas, C. G.; Tian, J.; Kovarik, L.; Jaegers, N. R.; Szanyi, J.; Wang, Y. Economizing on Precious Metals in Three-Way Catalysts: Thermally Stable and Highly Active Single-Atom Rhodium on Ceria for NO Abatement under Dry and Industrially Relevant Conditions**. *Angew. Chem., Int. Ed.* **2021**, *60*, 391−398.

(6) Kean, A. J.; Harley, R. A.; Littlejohn, D.; Kendall, G. R. On-Road Measurement of Ammonia and Other Motor Vehicle Exhaust Emissions. *Environ. Sci. Technol.* **2000**, *34*, 3535−3539.

(7) Kondarides, D. I.; Chafik, T.; Verykios, X. E. Catalytic Reduction of NO by CO over Rhodium Catalysts: 3. The Role of Surface Isocyanate Species. *J. Catal.* **2000**, *193*, 303−307.

(8) Takahashi, N.; Shinjoh, H.; Iijima, T.; Suzuki, T.; Yamazaki, K.; Yokota, K.; Suzuki, H.; Miyoshi, N.; Matsumoto, S.-i.; Tanizawa, T.; Tanaka, T.; Tateishi, S.-s.; Kasahara, K. The new concept 3-way

catalyst for automotive lean-burn engine: NOx storage and reduction catalyst. *Catal. Today* **1996**, *27*, 63−69.
(9) Epling, W. S.; Campbell, L. E.; Yezerets, A.; Currier, N. W.; Parks, J. E. Overview of the fundamental reactions and degradation mechanisms of NOx storage/reduction catalysts. *Catal. Rev.* **2004**, *46*, 163−245.
(10) US Environmental Protection Agency. National Air Quality: Status and Trends of Key Air Pollutants https://www.epa.gov/air-trends/air-quality-national-summary (accessed Nov 18 2020).
(11) Getsoian, A.; Theis, J. R.; Paxton, W. A.; Lance, M. J.; Lambert, C. K. Remarkable improvement in low temperature performance of model three-way catalysts through solution atomic layer deposition. *Nat. Catal.* **2019**, *2*, 614−622.
(12) Shelef, M.; Graham, G. W. Why Rhodium in Automotive Three-Way Catalysts? *Catal. Rev.* **1994**, *36*, 433−457.
(13) Taylor, K. C. Nitric oxide catalysis in automotive exhaust systems. *Catal. Rev.* **1993**, *35*, 457−481.
(14) Rasband, P. B.; Hecker, W. C. Catalyst characterization using quantitative FTIR: CO on supported Rh. *J. Catal.* **1993**, *139*, 551−560.
(15) Krenn, G.; Bako, I.; Schennach, R. CO adsorption and CO and O coadsorption on Rh(111) studied by reflection absorption infrared spectroscopy and density functional theory. *J. Chem. Phys.* **2006**, *124*, 144703.
(16) Jaworowski, A. J.; Beutler, A.; Strisland, F.; Nyholm, R.; Setlik, B.; Heskett, D.; Andersen, J. N. Adsorption sites in O and CO coadsorption phases on Rh(111) investigated by high-resolution core-level photoemission. *Surf. Sci.* **1999**, *431*, 33−41.
(17) Thiel, P. A.; Williams, E. D.; Yates, J. T.; Weinberg, W. H. The chemisorption of CO on Rh(111). *Surf. Sci.* **1979**, *84*, 54−64.
(18) Dubois, L. H.; Somorjai, G. A. The chemisorption of CO and CO_2 on Rh(111) studied by high resolution electron energy loss spectroscopy. *Surf. Sci.* **1980**, *91*, 514−532.
(19) Campbell, C.; White, J. M. The adsorption, desorption, and reactions of CO and O_2 on Rh. *J. Catal.* **1978**, *54*, 289−302.
(20) Root, T. W.; Schmidt, L. D.; Fisher, G. B. Nitric oxide reduction by CO on Rh(111): Temperature programmed reaction. *Surf. Sci.* **1985**, *150*, 173−192.
(21) Koch, H. P.; Singnurkar, P.; Schennach, R.; Stroppa, A.; Mittendorfer, F. A RAIRS, TPD, and DFT study of carbon monoxide adsorption on stepped Rh(553). *J. Phys. Chem. C* **2008**, *112*, 806−812.
(22) Linke, R.; Curulla, D.; Hopstaken, M. J. P.; Niemantsverdriet, J. W. CO/Rh(111): Vibrational frequency shifts and lateral interactions in adsorbate layers. *J. Chem. Phys.* **2001**, *115*, 8209−8216.
(23) Xu, J.; Yates, J. T. Terrace width effect on adsorbate vibrations: a comparison of Pt(335) and Pt(112) for chemisorption of CO. *Surf. Sci.* **1995**, *327*, 193−201.
(24) Fang, C.-Y.; Zhang, S.; Hu, Y.; Vasiliu, M.; Perez-Aguilar, J. E.; Conley, E. T.; Dixon, D. A.; Chen, C.-Y.; Gates, B. C. Reversible Metal Aggregation and Redispersion Driven by the Catalytic Water Gas Shift Half-Reactions: Interconversion of Single-Site Rhodium Complexes and Tetrarhodium Clusters in Zeolite HY. *ACS Catal.* **2019**, *9*, 3311−3321.
(25) Beniya, A.; Koitaya, T.; Kondoh, H.; Mukai, K.; Yoshimoto, S.; Yoshinobu, J. Adsorption and reaction of NO on the clean and nitrogen modified Rh(111) surfaces. *J. Chem. Phys.* **2009**, *131*, 084704.
(26) Wallace, W. T.; Cai, Y.; Chen, M. S.; Goodman, D. W. NO adsorption and dissociation on Rh(111): PM-IRAS study. *J. Phys. Chem. B* **2006**, *110*, 6245−6249.
(27) Nakamura, I.; Kobayashi, Y.; Hamada, H.; Fujitani, T. Adsorption behavior and reaction properties of NO and CO on Rh(111). *Surf. Sci.* **2006**, *600*, 3235−3242.
(28) Root, T. W.; Fisher, G. B.; Schmidt, L. D. Electron energy loss characterization of NO on Rh(111). I. NO coordination and dissociation. *J. Chem. Phys.* **1986**, *85*, 4679−4686.
(29) DeLouise, L. A.; Winograd, N. Adsorption and desorption of NO from Rh{111} and Rh{331} surfaces. *Surf. Sci.* **1985**, *159*, 199−213.
(30) Borg, H. J.; Reijerse, J. F. C. J. M.; van Santen, R. A.; Niemantsverdriet, J. W. The dissociation kinetics of NO on Rh(111) as studied by temperature programmed static secondary ion mass spectrometry and desorption. *J. Chem. Phys.* **1994**, *101*, 10052−10063.
(31) Permana, H.; Simon Ng, K. Y.; Peden, C. H. F.; Schmieg, S. J.; Lambert, D. K.; Belton, D. N. Adsorbed Species and Reaction Rates for NO−CO over Rh(111). *J. Catal.* **1996**, *164*, 194−206.
(32) Permana, H.; Ng, K. Y. S.; Peden, C. H. F.; Schmieg, S. J.; Belton, D. N. Effect of NO Pressure on the Reaction of NO and CO over Rh(111). *J. Phys. Chem.* **1995**, *99*, 16344−16350.
(33) Herman, G. S.; Peden, C. H. F.; Schmieg, S. J.; Belton, D. N. A comparison of the NO−CO reaction over Rh(100), Rh(110) and Rh(111). *Catalysis Letters* **1999**, *62*, 131.
(34) Renzas, J. R.; Zhang, Y.; Huang, W.; Somorjai, G. A. Rhodium nanoparticle shape dependence in the reduction of NO by CO. *Catal. Lett.* **2009**, *132*, 317−322.
(35) Oh, S.; Fisher, G. B.; Carpenter, J. E.; Goodman, D. W. Comparative kinetic studies of CO−O_2 and CO−NO reactions over single crystal and supported rhodium catalysts. *J. Catal.* **1986**, *100*, 360−376.
(36) Yang, C.; Garl, C. W. Infrared studies of carbon monoxide chemisorbed on rhodium. *J. Phys. Chem.* **1957**, *61*, 1504−1512.
(37) Yates, J. T.; Duncan, T. M.; Worley, S. D.; Vaughan, R. W. Infrared spectra of chemisorbed CO on Rh. *J. Chem. Phys.* **1979**, *70*, 1219−1224.
(38) Cavanagh, R. R.; Yates, J. T. Site distribution studies of Rh supported on Al_2O_3—An infrared study of chemisorbed CO. *J. Chem. Phys.* **1981**, *74*, 4150−4155.
(39) Hecker, W.; Bell, A. T. Reduction of NO by CO over silica-supported rhodium: infrared and kinetic studies. *J. Catal.* **1983**, *84*, 200−215.
(40) Solymosi, F.; Sárkány, J. An infrared study of the surface interaction between NO and CO on Rh/Al_2O_3 catalyst. *Appl. Surf. Sci.* **1979**, *3*, 68−82.
(41) Liang, J.; Wang, H. P.; Spicer, L. D. FT-IR study of nitric oxide chemisorbed on Rh/Al_2O_3. *J. Phys. Chem.* **1985**, *89*, 5840−5845.
(42) Granger, P.; Praliaud, H.; Billy, J.; Leclercq, L.; Leclercq, G. Infrared investigation of the transformation of NO over supported Pt- and Rh-based three-way catalysts. *Surf. Interface Anal.* **2002**, *34*, 92−96.
(43) Dujardin, C.; Mamede, A.-S.; Payen, E.; Sombret, B.; Huvenne, J. P.; Granger, P. Influence of the Oxidation State of Rhodium in Three-Way Catalysts on Their Catalytic Performances: An in situ FTIR and Catalytic Study. *Top. Catal.* **2004**, *30/31*, 347−352.
(44) Yik, E.; Hibbitts, D.; Wang, H.; Iglesia, E. Hydrogenation and C-S bond activation pathways in thiophene and tetrahydrothiophene reactions on sulfur-passivated surfaces of Ru, Pt, and Re nanoparticles. *Appl. Catal., B* **2021**, *291*, 119797.
(45) Hibbitts, D.; Dybeck, E.; Lawlor, T.; Neurock, M.; Iglesia, E. Preferential activation of CO near hydrocarbon chains during Fischer−Tropsch synthesis on Ru. *J. Catal.* **2016**, *337*, 91−101.
(46) Kravchenko, P.; Krishnan, V.; Hibbitts, D. Mechanism and Effects of Coverage and Particle Morphology on Rh-Catalyzed NO−H_2 Reactions. *J. Phys. Chem. C* **2020**, *124*, 13291−13303.
(47) Almithn, A. S.; Hibbitts, D. D. Supra-monolayer coverages on small metal clusters and their effects on H_2 chemisorption particle size estimates. *AIChE J.* **2018**, *64*, 3109−3120.
(48) Liu, J.; Hibbitts, D.; Iglesia, E. Dense CO adlayers as enablers of CO hydrogenation turnovers on Ru surfaces. *J. Am. Chem. Soc.* **2017**, *139*, 11789−11802.
(49) Loveless, B. T.; Buda, C.; Neurock, M.; Iglesia, E. CO chemisorption and dissociation at high coverages during CO hydrogenation on Ru catalysts. *J. Am. Chem. Soc.* **2013**, *135*, 6107−6121.

https://doi.org/10.1021/acs.jpcc.1c05160
J. Phys. Chem. C XXXX, XXX, XXX−XXX

(50) Deshlahra, P.; Conway, J.; Wolf, E. E.; Schneider, W. F. Influence of dipole-dipole interactions on coverage-dependent adsorption: CO and NO on Pt(111). *Langmuir* **2012**, *28*, 8408−8417.
(51) Curulla, D.; Linke, R.; Clotet, A.; Ricart, J. M.; Niemantsverdriet, J. W. Assignment of the vibrational features in the Rh(111)−(2×2)-3CO adsorption structure using density functional theory calculations. *Chem. Phys. Lett.* **2002**, *354*, 503−507.
(52) Curulla, D.; Linke, R.; Clotet, A.; Ricart, J. M.; Niemantsverdriet, J. W. A density functional study of the adsorption of CO on Rh(111). *Phys. Chem. Chem. Phys.* **2002**, *4*, 5372−5376.
(53) Dimakis, N.; Navarro, N. E.; Mion, T.; Smotkin, E. S. Carbon monoxide adsorption coverage study on platinum and ruthenium surfaces. *J. Phys. Chem. C* **2014**, *118*, 11711−11722.
(54) Fisher, I. A.; Bell, A. T. A Comparative Study of CO and CO_2 Hydrogenation over Rh/SiO_2. *J. Catal.* **1996**, *162*, 54−65.
(55) Kresse, G.; Furthmüller, J. Efficiency of ab-initio total energy calculations for metals and semiconductors using a plane-wave basis set. *Comput. Mater. Sci.* **1996**, *6*, 15−50.
(56) Kresse, G.; Hafner, J. Ab initio molecular-dynamics simulation of the liquid-metal−amorphous-semiconductor transition in germanium. *Phys. Rev. B: Condens. Matter Mater. Phys.* **1994**, *49*, 14251−14269.
(57) Kresse, G.; Hafner, J. Ab initio molecular dynamics for liquid metals. *Phys. Rev. B: Condens. Matter Mater. Phys.* **1993**, *47*, 558−561.
(58) Kresse, G.; Furthmüller, J. Efficient iterative schemes for ab initio total-energy calculations using a plane-wave basis set. *Phys. Rev. B: Condens. Matter Mater. Phys.* **1996**, *54*, 11169−11186.
(59) Kravchenko, P.; Plaisance, C.; Hibbitts, D. A new computational interface for catalysis. 2019, chemRxiv:8040737. Published as pre-print on https://chemrxiv.org/articles/preprint/8040737.
(60) Hammer, B.; Hansen, L. B.; Nørskov, J. K. Improved adsorption energetics within density-functional theory using revised Perdew-Burke-Ernzerhof functionals. *Phys. Rev. B: Condens. Matter Mater. Phys.* **1999**, *59*, 7413−7421.
(61) Perdew, J. P.; Burke, K.; Ernzerhof, M. Generalized gradient approximation made simple. *Phys. Rev. Lett.* **1996**, *77*, 3865−3868.
(62) Kresse, G.; Joubert, D. From ultrasoft pseudopotentials to the projector augmented-wave method. *Phys. Rev. B: Condens. Matter Mater. Phys.* **1999**, *59*, 1758−1775.
(63) Blöchl, P. E. Projector augmented-wave method. *Phys. Rev. B: Condens. Matter Mater. Phys.* **1994**, *50*, 17953−17979.
(64) Perdew, J. P.; Wang, Y. Accurate and simple analytic representation of the electron-gas correlation energy. *Phys. Rev. B: Condens. Matter Mater. Phys.* **1992**, *45*, 13244−13249.
(65) Wellendorff, J.; Lundgaard, K. T.; Møgelhøj, A.; Petzold, V.; Landis, D. D.; Nørskov, J. K.; Bligaard, T.; Jacobsen, K. W. Density functionals for surface science: Exchange-correlation model development with Bayesian error estimation. *Phys. Rev. B: Condens. Matter Mater. Phys.* **2012**, *85*, 235149.
(66) Kresse, G.; Hafner, J. Norm-conserving and ultrasoft pseudopotentials for first-row and transition elements. *J. Phys.: Condens. Matter* **1994**, *6*, 8245−8257.
(67) Vanderbilt, D. Soft self-consistent pseudopotentials in a generalized eigenvalue formalism. *Phys. Rev. B: Condens. Matter Mater. Phys.* **1990**, *41*, 7892−7895.
(68) Monkhorst, H. J.; Pack, J. D. Special points for Brillouin-zone integrations. *Phys. Rev. B: Solid State* **1976**, *13*, 5188−5192.
(69) Almithn, A.; Hibbitts, D. Effects of catalyst model and high adsorbate coverages in ab initio studies of alkane hydrogenolysis. *ACS Catal.* **2018**, *8*, 6375−6387.
(70) McQuarrie, D. A. *Statistical Mechanics*; University Science Books: Sausalito, California, 2000.
(71) Almithn, A. S.; Hibbitts, D. D. Impact of metal and heteroatom identities in the hydrogenolysis of C−X bonds (X = C, N, O, S, and Cl). *ACS Catal* **2020**, *10*, 5086.
(72) *NIST Chemistry WebBook, NIST Standard Reference Database Number 69*; Linstrom, P. J., Mallard, W. G., Eds.; National Institute of Standards and Technology: Gaithersburg, MD, 20899, 2020.
(73) Bergeret, G.; Gallezot, P. Particle size and dispersion measurements. *Handbook of Heterogeneous Catalysis: Online*; Ertl, G., Knözinger, H., Schüth, F., Weitkamp, J., Eds.; Wiley-VCH Verlag GmbH & Co. KGaA: Weinheim, Germany, 2008.
(74) Schennach, R.; Krenn, G.; Klötzer, B.; Rendulic, K. D. Adsorption of hydrogen and carbon monoxide on Rh(111)/V surface alloys. *Surf. Sci.* **2003**, *540*, 237−245.
(75) Wellendorff, J.; Silbaugh, T. L.; Garcia-Pintos, D.; Nørskov, J. K.; Bligaard, T.; Studt, F.; Campbell, C. T. A benchmark database for adsorption bond energies to transition metal surfaces and comparison to selected DFT functionals. *Surf. Sci.* **2015**, *640*, 36−44.
(76) Schmidt, P. S.; Thygesen, K. S. Benchmark Database of Transition Metal Surface and Adsorption Energies from Many-Body Perturbation Theory. *J. Phys. Chem. C* **2018**, *122*, 4381−4390.
(77) Köhler, L.; Kresse, G. Density functional study of CO on Rh(111). *Phys. Rev. B: Condens. Matter Mater. Phys.* **2004**, *70*, 165405.
(78) Castner, D. G.; Sexton, B. A.; Somorjai, G. A. LEED and thermal desorption studies of small molecules (H_2, O_2, CO, CO_2, NO, C_2H_4, C_2H_2 and C) chemisorbed on the Rhodium (111) and (100) surfaces. *Surf. Sci.* **1978**, *71*, 519−540.
(79) Fielicke, A.; von Helden, G.; Meijer, G.; Pedersen, D. B.; Simard, B.; Rayner, D. M. Size and charge effects on the binding of CO to small isolated rhodium clusters†. *J. Phys. Chem. B* **2004**, *108*, 14591−14598.
(80) Beutler, A.; Lundgren, E.; Nyholm, R.; Andersen, J. N.; Setlik, B. J.; Heskett, D. Coverage- and temperature-dependent site occupancy of carbon monoxide on Rh(111) studied by high-resolution core-level photoemission. *Surf. Sci.* **1998**, *396*, 117−136.
(81) Beutler, A.; Lundgren, E.; Nyholm, R.; Andersen, J. N.; Setlik, B.; Heskett, D. On the adsorption sites for CO on the Rh(111) single crystal surface. *Surf. Sci.* **1997**, *371*, 381−389.
(82) Gierer, M.; Barbieri, A.; Van Hove, M. A.; Somorjai, G. A. Structural reanalysis of the Rh(111) + ($\sqrt{3} \times \sqrt{3}$)R30°-CO and Rh(111) + (2 × 2)-3CO phases using automated tensor LEED. *Surf. Sci.* **1997**, *391*, 176−182.
(83) Avanesian, T.; Dai, S.; Kale, M. J.; Graham, G. W.; Pan, X.; Christopher, P. Quantitative and atomic-scale view of CO-induced Pt nanoparticle surface reconstruction at saturation coverage via DFT calculations coupled with in situ TEM and IR. *J. Am. Chem. Soc.* **2017**, *139*, 4551−4558.
(84) Kale, M. J.; Christopher, P. Utilizing Quantitative in Situ FTIR Spectroscopy to Identify Well-Coordinated Pt Atoms as the Active Site for CO Oxidation on Al_2O_3 -Supported Pt Catalysts. *ACS Catal.* **2016**, *6*, 5599−5609.
(85) Goldsmith, B. R.; Sanderson, E. D.; Ouyang, R.; Li, W.-X. CO- and NO-Induced Disintegration and Redispersion of Three-Way Catalysts Rhodium, Palladium, and Platinum: An ab Initio Thermodynamics Study. *J. Phys. Chem. C* **2014**, *118*, 9588−9597.
(86) Ouyang, R.; Liu, J.-X.; Li, W.-X. Atomistic theory of Ostwald ripening and disintegration of supported metal particles under reaction conditions. *J. Am. Chem. Soc.* **2013**, *135*, 1760−1771.
(87) Matsubu, J. C.; Yang, V. N.; Christopher, P. Isolated metal active site concentration and stability control catalytic CO_2 reduction selectivity. *J. Am. Chem. Soc.* **2015**, *137*, 3076−3084.
(88) Hadjiivanov, K. I.; Vayssilov, G. N. Characterization of oxide surfaces and zeolites by carbon monoxide as an IR probe molecule. *Advances in Catalysis*; Elsevier, 2002; Vol. *47*, pp 307−511.
(89) Gruver, V.; Fripiat, J. J. Lewis acid sites and surface aluminum in aluminas and mordenites: an infrared study of CO chemisorption. *J. Phys. Chem.* **1994**, *98*, 8549−8554.
(90) Almusaiteer, K. A.; Chuang, S. S. C. Infrared Characterization of Rh Surface States and Their Adsorbates during the NO−CO Reaction. *J. Phys. Chem. B* **2000**, *104*, 2265−2272.
(91) Anderson, J. A. CO oxidation on Rh/Al_2O_3 catalysts. *Faraday Trans.* **1991**, *87*, 3907.
(92) Van't Blik, H. F. J.; Van Zon, J. B. A. D.; Huizinga, T.; Vis, J. C.; Koningsberger, D. C.; Prins, R. Structure of rhodium in an ultradispersed rhodium/alumina catalyst as studied by EXAFS and other techniques. *J. Am. Chem. Soc.* **1985**, *107*, 3139−3147.

https://doi.org/10.1021/acs.jpcc.1c05160
J. Phys. Chem. C XXXX, XXX, XXX−XXX

(93) de Jong, A. M.; Niemantsverdriet, J. W. The adsorption of CO on Rh(100): Reflection absorption infrared spectroscopy, low energy electron diffraction, and thermal desorption spectroscopy. *J. Chem. Phys.* **1994**, *101*, 10126−10133.
(94) Leung, L. W. H.; He, J. W.; Goodman, D. W. Adsorption of CO on Rh(100) studied by infrared reflection−absorption spectroscopy. *J. Chem. Phys.* **1990**, *93*, 8328−8336.
(95) Dean, J.; Taylor, M. G.; Mpourmpakis, G. Unfolding adsorption on metal nanoparticles: Connecting stability with catalysis. *Sci. Adv.* **2019**, *5*, No. eaax5101.
(96) Li, H.; Rivallan, M.; Thibault-Starzyk, F.; Travert, A.; Meunier, F. C. Effective bulk and surface temperatures of the catalyst bed of FT-IR cells used for in situ and operando studies. *Phys. Chem. Chem. Phys.* **2013**, *15*, 7321−7327.
(97) Cheula, R.; Maestri, M.; Mpourmpakis, G. Modeling morphology and catalytic activity of nanoparticle ensembles under reaction conditions. *ACS Catal.* **2020**, *10*, 6149−6158.
(98) Shustorovich, E. The UBI-QEP method: A practical theoretical approach to understanding chemistry on transition metal surfaces. *Surf. Sci. Rep.* **1998**, *31*, 1−119.
(99) Hammer, B.; Nielsen, O. H.; Nrskov, J. K. Structure sensitivity in adsorption: CO interaction with stepped and reconstructed Pt surfaces. *Catal. Lett.* **1997**, *46*, 31−35.
(100) Peterson, A. A.; Grabow, L. C.; Brennan, T. P.; Shong, B.; Ooi, C.; Wu, D. M.; Li, C. W.; Kushwaha, A.; Medford, A. J.; Mbuga, F.; Li, L.; Nørskov, J. K. Finite-Size Effects in O and CO Adsorption for the Late Transition Metals. *Top. Catal.* **2012**, *55*, 1276−1282.
(101) Freel, J. Chemisorption on supported platinum I. Evaluation of a pulse method. *J. Catal.* **1972**, *25*, 139−148.
(102) Kip, B.; Duivenvoorden, F. B. M.; Koningsberger, D. C.; Prins, R. Determination of metal particle size of highly dispersed Rh, Ir, and Pt catalysts by hydrogen chemisorption and EXAFS. *J. Catal.* **1987**, *105*, 26−38.
(103) Schumann, M.; Nielsen, M. R.; Smitshuysen, T. E. L.; Hansen, T. W.; Damsgaard, C. D.; Yang, A.-C. A.; Cargnello, M.; Grunwaldt, J.-D.; Jensen, A. D.; Christensen, J. M. Rationalizing an Unexpected Structure Sensitivity in Heterogeneous Catalysis—CO Hydrogenation over Rh as a Case Study. *ACS Catal.* **2021**, *11*, 5189−5201.
(104) Wang, L.; Zeng, Z.; Gao, W.; Maxson, T.; Raciti, D.; Giroux, M.; Pan, X.; Wang, C.; Greeley, J. Tunable intrinsic strain in two-dimensional transition metal electrocatalysts. *Science* **2019**, *363*, 870−874.
(105) Jørgensen, M.; Grönbeck, H. Strain Affects CO Oxidation on Metallic Nanoparticles Non-linearly. *Top. Catal.* **2019**, *62*, 660.
(106) Khorshidi, A.; Violet, J.; Hashemi, J.; Peterson, A. A. How strain can break the scaling relations of catalysis. *Nat. Catal.* **2018**, *1*, 263−268.
(107) Eren, B.; Zherebetskyy, D.; Patera, L. L.; Wu, C. H.; Bluhm, H.; Africh, C.; Wang, L.-W.; Somorjai, G. A.; Salmeron, M. Activation of Cu(111) surface by decomposition into nanoclusters driven by CO adsorption. *Science* **2016**, *351*, 475−478.
(108) Tao, F.; Dag, S.; Wang, L.-W.; Liu, Z.; Butcher, D. R.; Bluhm, H.; Salmeron, M.; Somorjai, G. A. Break-up of stepped platinum catalyst surfaces by high CO coverage. *Science* **2010**, *327*, 850−853.
(109) Tao, F.; Dag, S.; Wang, L.-W.; Liu, Z.; Butcher, D. R.; Salmeron, M.; Somorjai, G. A. Restructuring of hex-Pt(100) under CO gas environments: formation of 2-D nanoclusters. *Nano Lett.* **2009**, *9*, 2167−2171.
(110) Somorjai, G. A.; Van Hove, M. A. Adsorbate-induced restructuring of surfaces. *Prog. Surf. Sci.* **1989**, *30*, 201−231.
(111) Somorjai, G. A.; Hwang, K. S.; Parker, J. S. Restructuring of hydrogenation metal catalysts under the influence of CO and H_2. *Top. Catal.* **2003**, *26*, 87−99.
(112) Anderson, J. A.; Millar, G. J.; Rochester, C. H. Infrared study of the adsorption of NO, NO_2 and CO on Rh/Al_2O_3 catalysts. *Faraday Trans.* **1990**, *86*, 571.
(113) Root, T. W.; Fisher, G. B.; Schmidt, L. D. Electron energy loss characterization of NO on Rh(111). II. Coadsorption with oxygen and CO. *J. Chem. Phys.* **1986**, *85*, 4687−4695.
(114) Altman, E.; Gorte, R. J. A temperature-programmed desorption study of NO on Rh particles supported on α-Al_2O_3 {0001}. *J. Catal.* **1988**, *113*, 185−192.
(115) Zafiris, G.; Gorte, R. J. Adsorption of NO and CO on $Rh/ZrO_2(100)$. *J. Catal.* **1991**, *132*, 275−286.
(116) Matsumura, Y.; Koda, Y.; Yamada, H.; Shigetsu, M.; Takami, A.; Ishimoto, T.; Kai, H. Experimental and Computational Studies of CO and NO Adsorption Properties on Rh-Based Single Nanosized Catalysts. *J. Phys. Chem. C* **2020**, *124*, 2953−2960.
(117) Keiski, R. L.; Härkönen, M.; Lahti, A.; Maunula, T.; Savimäki, A.; Slotte, T. An infrared study of CO and NO adsorption on Pt, Rh, Pd 3-way catalysts. *Catalysis and Automotive Pollution Control III, Proceedings of the Third International Symposium Capoc 3*; *Studies in surface science and catalysis*; Elsevier, 1995; Vol. *96*, pp 85−96.

https://doi.org/10.1021/acs.jpcc.1c05160
J. Phys. Chem. C XXXX, XXX, XXX−XXX